This project has received funding from the European Union's Seventh Programme for research, technological development and demonstration under grant agreement No [308417]".

New Directions in Seismic Hazard Assessment through Focused Earth Observation in the Marmara Supersite

Grant Agreement Number: 308417
co-funded by the European Commission within the Seventh Framework Programme
THEME [ENV.2012.6.4-2]
[Long-term monitoring experiment in geologically active regions of Europe prone to natural hazards: the Supersite concept]

D7.1

Report on the re-evaluation of the seismo-tectonics and geo-hazards of the Marmara region

Project Start Date	1 November 2012
Project Duration	42 months
Project Coordinator /Organization	Nurcan Meral Özel / KOERI
Work Package Number	WP 7
Deliverable Name/ Number	Report on the re-evaluation of the seismo-tectonics and geo-hazards of the Marmara region/D 7.1
Due Date Of Deliverable	30 April 2016
Actual Submission Date	2 May2016
Organization/Author (s)	CNRS / Pierre Henry

Dissemination Level		
PU	Public	▨
PP	Restricted to other programme participants (including the Commission)	
RE	Restricted to a group specified by the consortium (including the Commission)	
CO	Confidential, only for members of the consortium (including the Commission)	

CONTENTS

Abstract

In the Sea of Marmara and Istanbul area, the 24±1 mm/yr plate velocity between Anatolia and Eurasia is distributed over at least two branches of the North Anatolian Fault (NAF) system. The average rate of extension across the Sea of Marmara is about 2.5 mm/yr. If applied continuously during 5 Ma, this rate could account for the crustal thinning found below the deep basins of the Sea of Marmara and the southern shelf. Since at least 2 Ma, the growth of the deep basins is coupled with slip along the Northern Branch of the NAF, which currently takes up more than 10 mm/yr of strike-motion, while other individual faults strands accommodate a few mm/yr at most. Istanbul is mostly exposed to earthquakes occurring on the Northern Branch of the NAF. However, the Southern fault system (which comprises Gemlik Fault) as well as offshore splays of the Northern Branch (e.g. Imrali Basin Fault and Marmara Island Fault) are potential sources of damaging earthquakes with a longer recurrence time interval.

Based on on-land studies, geological slip rate on the Northern Branch likely ranges between 14 and 19 mm/yr representing about 2/3 to 3/4 of plate motion. The uncertainty on the geological slip rate remains larger on offshore fault strands because of uncertainties in stratigraphic age models. Sediment coring performed during MARSITECRUISE will improve the age models over the last 100 000 years, but deeper coring is needed, and envisioned within framework of IODP.

Slip deficit and earthquake recurrence intervals also depend on the amount of aseismic creep that may be occurring on a given segment. The loading rate on offshore fault strands is not precisely known, and creep could be significant for the western (Ganos - Central Basin) and central (Istanbul - Silivri) segments. In an effort to better constrain the slip deficit and earthquake recurrence interval on the central segment, acoustic distance meters were deployed at the seafloor and sediment cores were taken in Kumburgaz Basin for paleoseismological studies.

Synthesis report

1. Introduction

At the beginning of the MARSITE project questions were posed regarding (1) the evolution of the tectonic framework and fault network with time; (2) slip partitioning and slip rate on individual fault segments; (3) geodetic vs. geologic rates. Specific actions were taken in Task 1 of WP 7 to provide answers. Results were obtained based on existing data sets and are now published (Sengor et al., 2014; Grall et al., 2013, 2014; Gorur et al., 2013). A cruise of Ifremer N/O "Pourquoi Pas ?" (MARSITECRUISE, October 28th – November 17th) was planned within the MARSITE framework and acquired new data relevant for WP7 objectives, such as gravity data and sediment core samples. These data sets are still being analyzed. One article based on MARSITECRUISE gravity data has been submitted and is being revised (Kende et al., see manuscript in Annex). The present report summarizes the questions addressed, their context, and the progress made within the timeframe of Marsite.

2. Tectonic evolution of the Sea of Marmara

The initiation of the North Anatolian fault in the Sea of Marmara is preceded by deformation affecting the Eocene-Oligocene Thrace basin. The age of initiation of the North Anatolian Fault is known to decrease westward from Mid Miocene at its eastern end to Pliocene in the Sea of Marmara region, but where and how the motion between Eastern Anatolia and Europe were accommodated is not well known. Work within MARSITE characterized deformation in the Thrace basin and examined its relationships with the North Anatolian Fault (Gorur et al., 2013). This study concludes that deformation affecting the Thrace Basin peaked during the Late Miocene to Early Pliocene.

Crustal thinning in the Sea of Marmara area is related to the history of North Anatolian Fault initiation and strike-slip basin formation. Seismic reflection and refraction studies showed an uplifted Moho beneath the deep basin and imaged crustal detachements and tilted bloc systems (Becel et al., 2009), but no quantification of extension was attempted. Gravity modeling performed within MARSITE aimed to determine the geometry of the Moho, crustal thickness and the amount of extension. Gravity data collected during MARSITECRUISE were merged with a global gravity model derived from satellite altimetry. The gravity anomaly was corrected for topography and basin geometry, and an inversion performed to obtain Moho depth, also taking into account constraints from seismic refraction and receiver function studies. An article was submitted to JGR and is currently under revision. Extension thus determined amounts to 2100±300 km^2 —or 13±2 km averaged over the 160 km length of the Sea of Marmara— and would thus correspond to an obliquity of 9-15° considering a total strike-slip offset ranging from 50 to 90 km (Akbayram et al., 2015). At the present rate of areal extension derived from GPS data, about 5 Ma would be needed to explain the observed crustal thinning, which is probably slightly older than the onset of deformation related to the North Anatolian Fault. Extension may, however, have peaked in the early Pliocene if the westward progression of the strike-slip plate boundary was associated with a purely extensional episode, analogous to the present day Corinth Gulf (Le Pichon et al., 2015). It is also found that the zone of Moho uplift is wider than the deep basins and extends below the shelf. This may be a consequence of this early extension phase, of ductile lower crustal flow or a combination of both.

The currently active fault system only comprises a fraction of the faults that have been active since the initiation of the North Anatolian Fault, and this situation may account for the initial diversity of tectonic interpretations in the Sea of Marmara. Interpretations of seismic and bathymetric data have now largely converged to a scheme with a master fault —connecting the Izmit segment that ruptured in 1999 with the Ganos segment that ruptured in 1912— and subsidiary fault branches (e.g. Le Pichon et al., 2001; Armijo et al., 2002; Demirbag et al. 2003; Armijo et al., 2005; Rangin et al., 2004; Seeber et al., 2004, 2006). Remaining differences come in part from the characteristics of the data sets used, and notably resolution and depth of investigation of seismic data. One objective of MARSITE WP7 work was to clarify which faults are cutting the seafloor (and thus currently active) and which ones do not. Several now inactive (or marginally active) fault systems appear to have played a role in the structuring of the basins. This is for example the case for the system of extensional detachments and tilted blocs between the southern shelf and the deep basins (Becel et al., 2009) for the South Marmara Fault, connecting the Gemlik Bay to the Dardanelles (Le Pichon et al., 2013) and for an en-echelon system lying in prolongation of the Izmit fault (Grall et al., 2012). On the other hand several arrays of normal faults observed at a shallow level in the sediment are not deeply rooted, and could result from the interaction of slope instability with underlying crustal deformation (Zitter et al., 2012). Existing seismic profiles were re-examined to draw an updated structural map (Sengor et al., 2014). While a tendency is observed toward strain localization in a 7-to-10 km swath along the Main Marmara Fault, it is also evident that some deformation is still accommodated over a broader area, and that subsidiary faults display a complex history of fault activation/deactivation (Sengor et al. 2014).

The currently active fault system was established some time between 2 Ma and 500.000 years, more likely through a progressive reorganization related to basin growth than as a sudden event (Grall et al., 2012, Sorlien et al., 2012). No major change of tectonic regime at the scale of the Sea of Marmara is required over the last 400.000 years, although local variations in the rates of subsidence/uplift and in the strain distribution around the main fault are documented (Grall et al., 2012; 2013). Accurate dating of stratigraphic horizons and tectonic event is still difficult in the Sea of Marmara because constrains from boreholes are very limited. However, efforts to ground truth and upper most seismic horizons (attributed to age 100,000 250,000 330,000 and 450,000 years) with long (Calypso) piston corers during MARSITECRUISE have been largely successful. We will come back to this point in the fault rate section.

The GIS fault map provided as MARSITE deliverable D7.2 is based primarily on multichannel data and thus represents the fault geometry at a few kilometers depth within the syntectonic basins (Sengor et al., 2014). Faults are categorized as deep-rooted faults that also cut through the seafloor, blind faults, and shallow syn-sedimentary faults. For the purpose of hazard assessment, information from sediment sounder profiles and high-resolution bathymetry is essential to assess fault activity and deformation style, but the geometry that should preferentially be considered for the construction of earthquake scenarios is the geometry of the faults at crustal level. However, crustal structure is poorly imaged below the Sea of Marmara Basin and, so far, three-dimensional fault geometry at depths (Hergert et al., 2010, 2011) is largely inferred from seismic imaging in the syntectonic basins (Becel et al., 2010; Carton et al., 2007). Fault models may be further constrained taking relocated seismicity into consideration (Bulut et al., 2009; Karabulut et al., 2011; Schmittbuhl et al., 2015).

3. Geological fault slip rates

Geological strike-slip rates determined on the northern branch of the northern branch of the NAF on land appear compatible with the more recent determinations in the Sea of Marmara. From a compilation of published results, Hergert et al. (2011) concluded that the possible range of geological slip rate for the North Anatolian Fault northern branch is 14-19 mm/yr, which is not significantly lower than the 18 ± 3.5 mm/yr estimated for the central and eastern NAF (Hubert-Ferrari et al., 2002). More recent studies remain within this range. For example, trenching studies in Ganos find a slip rate of 17±5 mm/yr over the last 1000 years with an average earthquake recurrence interval of 323±142

(Meghraoui et al., 2012). On the other hand, estimations based on geomorphic features offset by the NAF strands after their abandonment related to the post-glacial sea level rise yielded much lower slip rates in Izmit Gulf as well as in Saros Gulf (Polonia et al., 2004; Gasperini et al., 2011a). The 10 mm/yr rate obtained by these studies is, however, difficult to reconcile with models of Cinarcik basin growth, that bracket the strike-slip rate between 12.6 and 29 mm/yr, with a preferred value at 18.5 mm/yr (Kurt et al., 2013)(Figure 1). Arguably, occurrence of distributed deformation in soft sediments may cause observations at the seafloor to underestimate the geological slip rate on a fault. First, rupture at the surface during an earthquake may only represent a fraction of the slip at depth on the same fault. For example, in the Izmit Gulf, radar interferometry indicate some coseismic slip occurred at depth all the way to the western entrance of the Gulf, but evidence for surface rupture in this area is very patchy (Gasperini et al., 2011b; Çakir et al., 2003). Moreover, strain accommodated by small faults, folding and ductile deformation in soft, high porosity sediment is difficult to evaluate. This may contribute to explain the relatively low rates obtained from offset morphology in Izmit Gulf and Saros Gulf as well as on the Sea of Marmara Central High.

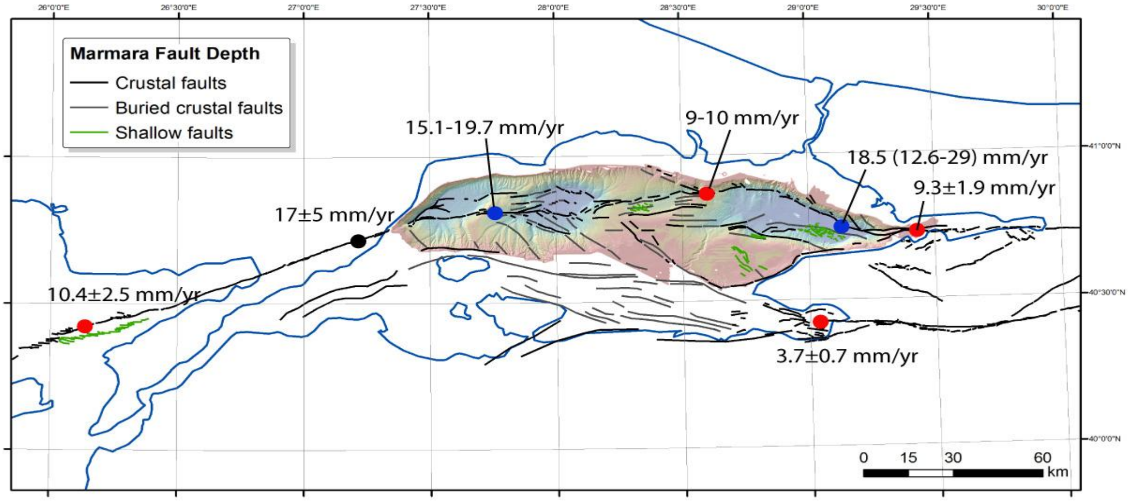

Figure 1: Fault map showing distinction between faults with seafloor expression and rooted in the crust, faults without seafloor expression (blind or buried), and shallow faults. The shallow faults, may be associated with underlying crustal deformation, but do not correspond to a deep fault having the same geometry and style as the fault forming the seafloor scarps. Fault rates from trenching studies are indicated in black (Meghraoui

et al., 2012); from Holocene offsets in red (this study and Gasperini et al., 2009); from Pleistocene stratigraphic correlations in blue (Grall et al., 2013; Kurt et al., 2013)

Work performed within Marsite included the identification of offset sedimentary bodies in a 3D HR seismic data set acquired by Ifremer along the Main Marmara Fault on the western high. Three mass transport deposit complexes were identified and one of them yielded a measurable offset across the fault of 7.7±0.3 km, corresponding to a slip velocity range of 15.1–19.7mm/a over the last 405–490 ka (Grall et al., 2013). Attempts to identify reliable piercing points in the sedimentary structure and measure fault offset on the basis of 2D seismic or chirp lines were not successful. Acquisition of 3D HR data at other locations would be necessary quantify geological fault slip rates at other locations offshore. Offset submarine gullies presumably abandoned after the post-glacial sea-level rise were however, found, notably on the Central High SW slope. The slip rate estimated from these offsets is in the 9-to-10-mm/yr-range, comparable with the slip rate estimates in Izmit and Saros Gulf. It thus appears that there is a systematic bias between slip rate estimates based on post-glacial abandonment surfaces (last 12000 years) and from stratigraphic interpretations of Late Pliocene sequences (100,000 yr to 500,000 years time scale). There is little uncertainty on the maximum age of the paleo-shoreline described in Izmit Gulf (Polonia et al., 2004), as the timing of reconnection of the Sea of Marmara with the Mediterranean is well constrained from coring (Vidal et al., 2010). However, the age assigned to the deeper reflectors still has to be confirmed as it is based on sequence stratigraphy interpretation of seismic profiles and sediment rate extrapolations.

Ground truthing of key horizons by coring is thus needed to confirm Late Pleistocence stratigraphic age models and fault slip rates, and was added among the objectives of WP7. During MARSITECRUISE, 9 cores of length 9 m to 21 m were taken for this purpose. Cores were accurately correlated with seismic data and sediment sounder profiles. A horizon referred to as red-H1 with an age estimated c.a. 100.000 year (corresponding to the last interglacial) (Sorlien et al., 2012; Grall et al., 2013) was successfully cored at least at 4 locations. Core descriptions suggest this reflector in fact corresponds to the transition from Marine Isotope Stage (MIS) 5 to 4, and thus would be slightly younger than expected. This however, still needs to be confirmed by further analysis. Deeper horizons corresponding to older marine high stands (MIS 7 or 9) where reached at least at two locations, but their age still needs to be determined. Deeper coring is envisioned in the future through IODP drilling.

Slip rates on active faults on the North Anatolian Fault zone vary over several orders of magnitude between the main fault branch, subsidiary faults branches, and minor faults. By active fault, Late Pleistocene to Holocene fault displacement is meant. In the marine domain, evidence of activity can be the presence of a fault scarp at the seafloor, or an offset of shallow seismic reflectors. Important horizons for assessing fault activity are the Lacustrine-Marine transition horizon, observable on sediment sounder profiles in most basins, and the red-H1 horizon (interpreted as the end of the last interglacial), which has been correlated over topographic highs and basins throughout the Sea of Marmara (Sorlien et al., 2012; Grall et al., 2013). In addition, blind faults may be considered to have some level of activity if microseismicity is present along them. However, no distinction is made from geomorphic observation between co-seismic deformation and aseismic deformation, which may be related to fault creep at depths.

There are few strike-slip rate determinations on other submarine faults that the MMF. A strike-slip rate of 3.7±0.7 mm/yr was determined on Gemlik Fault from post-glacial topographic offset (Gasperini et al., 2011 a). Gemlik Fault is part of the southern NAF system but its westward prolongation, and connection to faults on land, is still not fully described. A classification is proposed based on the order of magnitude of slip rate and included as a fault attribute in the GIS database (Figure 2). Fault slip rate categories are (A) more than 10 mm/yr, (B) 1-10 mm/yr, (C) 0.1-1 mm/yr, (D) less than 0.1 mm/yr. In most cases in the marine domain vertical offset of the seafloor or reflectors is the only information available to evaluate the level of activity of a fault. For instance on a normal fault, the displacement since the lacustrine-marine transition should be more than 120 m for category (A), more than 12 m for category (B), 1.2 m for category (C), more than 12 cm for category (D), which is close to the resolution of sediment sounder profiles. At the level of the red-H1, a 1-10 m offset observed near the resolution limit of seismics would imply a classification in category (C). (D) Thus includes faults having an unclear level of activity. Strike slip faults can cause apparent offset of surface of reflectors when the fault motion comprises a vertical component or when it intersects a slope, which can indicate the probable category of the fault, but is not a measure of its rate. The surface expression of a fault is also strongly dependant on the sedimentation rate as faults should produce relative vertical displacements of the same order of the sedimentation rate to form a scarp at the seafloor. It follows that faults forming scarps in the basins, where sedimentation rate is more than 1 mm/yr, generally fall is categories (A) and (B) whereas on the structural highs, many more faults are observed in categories (C) and (D).

All segments of the Main Marmara Fault are considered in category (A) because the lowest geological slip rate determination on this fault is 10 mm/yr (Gasperini et al., 2010; Grall et al., 2012; Kurt et al., 2013). Category (B) include relatively few faults, corresponding at crustal level to subsidiary faults branches included in the mechanical model of Heidbach et al. (2011). It appears that many faults with significant geomorphologic expression end in category (D). Some of the fault in category (C) produced vertical offsets of several hundred meters to kilometers in the 500.000 to 5 Ma time frame of basin formation in the Sea of Marmara, but it often remains difficult to determine whether this is the result of episodic activity or of steady-state slow motion.

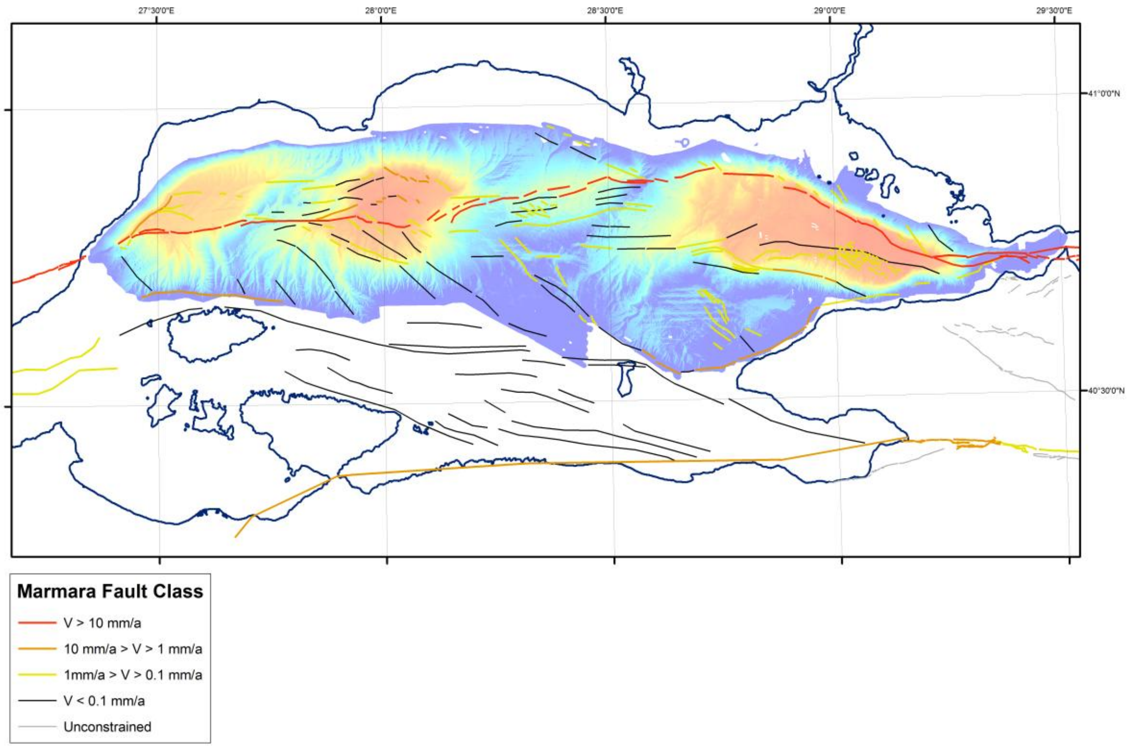

Figure 2: Classification of faults in the Sea of Marmara based on order of magnitude of slip velocity. Fault geometry based on Sengor et al. (2013).

4. Comparison of geological rates and geodetic rates

The relative motion between Anatolia and Europe is well constrained from space geodesy (e.g. Reilinger et al., 2006, 2010) and amounts to 24±1 mm/yr right lateral strike-slip motion on the North Anatolian Fault. The North Anatolian fault system divides westward into a northern fault branch crossing the Sea of Marmara between Izmit Gulf and Ganos a Southern fault system, which itself comprises the Gemlik fault and its offshore prolongation (the Middle Branch) as well as Southern Branch. The strain partitioning between the two systems is such that the northern fault branch takes up most of the strike-slip component of plate motion while the southern fault system accommodates oblique extension (Flerit et al., 2003, 2004; Reilinger, 2006). Within the offshore part of the northern fault system, partitioning between the Main Marmara Fault and the subsidiary fault branches cannot be constrained from geodesy, but mechanical modeling suggests that the slip rate on the Main Marmara Fault may vary laterally in the 14-19 mm/yr range, and thus would represent only a fraction of the full plate motion (Herger et al., 2010, 2011).

Fault slip rate on the main fault segments both onland and offshore appear to be only about 2/3 to 3/4 of plate motion, which leaves the possibility that subsidiary faults could cause damaging earthquakes, although of lower magnitude and with longer recurrence interval. The Duzce earthquake (1999) may be considered as one such case and the same situation may also arise on other segments of the NAF where slip may not occur on a single strand (Zabcı et al., 2015). In the Sea of Marmara area the potential of the Southern NAF branch (which comprises the Gemlik fault) is well considered. The Marmara Island fault is also known to have potential for earthquake of magnitude 6.4-6.6 (Altinok et al., 2006). The question may be asked for the Imrali basin faults and perhaps also for relicts of the South Marmara Fault, although no historical earthquake has been assigned to these fault systems. As part of WP7 activities, a core has been taken in Imrali basin during MARSITECRUISE for paleoseismological studies and is being studied at ITU.

Silent slip on faults may impact estimates of slip deficit and thus earthquake scenarios (slip and recurrence interval) and probability of occurrence. Creep on some intervals of the NAF on land is known to occur as long-term post-seismic motion, affecting shallow parts of fault segments which slipped co-seismically, notably within the rupture zone of Izmit earthquake (Çakir et al., 2011). Measuring fault creep offshore is a challenge. The low, or absence of, interseismic loading in the Istanbul area at about 10 km distance from the fault is puzzling (Ergintav et al., 2014; Le Pichon et al., 2003). Possible explanations involve asymmetry in crustal elastic properties north and south of the fault (Le Pichon et al., 2003), creep at near plate velocity (Ergintav et al., 2014; see WP3), or a very shallow locked zone (less than 5 km). The shallow locked zone explanation may however be considered unlikely considering the depth distribution of microseismicity (Schmittbuhl et al., 2014; see WP4). Distribution of seismicity suggests that some creep occurs in the western Sea of Marmara from Ganos to the Central Basin. The need to better constrain fault creep offshore lead to coordinate within the framework of MARSITE WP8 and EMSO ERIC the deployment of acoustic ranging beacons on the

Istanbul segment in order to measure and monitor creep. Within MARSITE WP7, sediment cores for paleoseismological studies were taken in the Kumburgaz basin segment in order to clarify earthquake recurrence interval on the Istanbul segment, and are being studied at ITU.

5. List of Marsite WP7 Task 1 publications

Görür, N., and Ş. Elbek (2013), Tectonic events responsible for shaping the Sea of Marmara and its surrounding region, *Geodin. Acta*, (January), 1–11, doi:10.1080/09853111.2013.859346.

Grall, C., P. Henry, Y. Thomas, G. K. Westbrook, M. N. Çağatay, B. Marsset, H. Saritas, G. Çifçi, and L. Géli (2013), Slip rate estimation along the western segment of the main marmara fault over the last 405-490 ka by correlating mass transport deposits, *Tectonics*, *32*, 1587–1601, doi:10.1002/2012TC003255.

Şengör, A. M. C., C. Grall, C. İmren, X. Le Pichon, N. Görür, P. Henry, H. Karabulut, and M. Siyako (2014), The geometry of the North Anatolian transform fault in the Sea of Marmara and its temporal evolution: implications for the development of intracontinental transform faults 1, *Can. J. Earth Sci.*, *51*(3), 222–242, doi:10.1139/cjes-2013-0160.

Kende, J., P. Henry, G. Bayrakci, S. Ozeren, C. Grall, Moho depth and crustal thinning in the Marmara Sea region from gravity data inversion, *J. Geophys. Res.*, in revision.

6. Cited References

Akbayram, K., C. C. Sorlien, and A. I. Okay (2016), Evidence for a minimum 52±1km of total offset along the northern branch of the North Anatolian Fault in northwest Turkey, *Tectonophysics*, *668-669*, 35–41, doi:10.1016/j.tecto.2015.11.026.

Altınok, Y., and B. Alpar (2006), Marmara Island earthquakes, of 1265 and 1935; Turkey, Nat. Hazards Earth Syst. Sci., 6, 999–1006, doi:10.5194/nhess-6-999-2006. Bohnhoff, M., F. Bulut, G. Dresen, P. E. Malin, T. Eken, and M. Aktar (2013), An earthquake gap south of Istanbul., *Nat. Commun.*, *4*(May), 1999, doi:10.1038/ncomms2999.

Armijo, R., B. Meyer, S. Navarro, G. King, and A. Barka (2002), Asymmetric slip partitioning in the sea of Marmara pull-apart: A clue to propagation processes of the North Anatolian Fault?, *Terra Nov.*, *14*, 80–86, doi:10.1046/j.1365-3121.2002.00397.x.

Armijo, R. et al. (2005), Submarine fault scarps in the Sea of Marmara pull-apart (North Anatolian Fault): Implications for seismic hazard in Istanbul, *Geochemistry, Geophys. Geosystems*, *6*, 1–29, doi:10.1029/2004GC000896.

Bécel, A., M. Laigle, B. de Voogd, A. Hirn, T. Taymaz, S. Yolsal-Cevikbilen, and H. Shimamura (2010), North Marmara Trough architecture of basin infill, basement and faults, from PSDM reflection and OBS refraction seismics, *Tectonophysics*, *490*, 1–14, doi:10.1016/j.tecto.2010.04.004.

Bulut, F., M. Bohnhoff, W. L. Ellsworth, M. Aktar, and G. Dresen (2009), Microseismicity at the North Anatolian Fault in the Sea of Marmara offshore Istanbul, NW Turkey, *J. Geophys. Res. Solid Earth*, *114*, 1–16, doi:10.1029/2008JB006244.

Çagatay, M. N., S. Wulf, Ü. Sancar, L. Vidal, P. Henry, O. Appelt, and L. Gasperini (2015), The tephra record from the Sea of Marmara for the last ca . 70 ka and its palaeoceanographic implications, *Mar. Geol.*, *361*, 96–110, doi:10.1016/j.margeo.2015.01.005.

Çakir, Z., S. Ergintav, H. Özener, U. Dogan, A. M. Akoglu, M. Meghraoui, and R. Reilinger (2012), Onset of aseismic creep on major strike-slip faults, *Geology*, *40*, 1115–1118, doi:10.1130/G33522.1.

Çakir, Z., J. B. de Chabalier, R. Armijo, B. Meyer, A. Barka, and G. Peltzer (2003), Coseismic and early post-seismic slip associated with the 1999 Izmit earthquake (Turkey), from SAR interferometry and tectonic field observations, Geophys. J. Int., 155(1), 93–110, doi:10.1046/j.1365-246X.2003.02001.x.

Ergintav, S., R. Reilinger, R. Çakmak, M. Floyd, Z. Çakir, U. Doğan, R. W. King, S. Carton, H. et al. (2007), Seismic imaging of the three-dimensional architecture of the Çınarcık Basin along the North Anatolian Fault, *J. Geophys. Res. Solid Earth*, *112*, 1–17, doi:10.1029/2006JB004548.

McClusky, and H. Özener (2014), Istanbul's earthquake hot spots: Geodetic constraints on strain accumulation along faults in the Marmara seismic gap, Geophys. Res. Lett., 41, doi:10.1002/2014GL060985.

Flerit, F., R. Armijo, G. C. P. King, B. Meyer, and a. Barka (2003), Slip partitioning in the Sea of Marmara pull-apart determined from GPS velocity vectors, *Geophys. J. Int.*, *154*, 1–7, doi:10.1046/j.1365-246X.2003.01899.x.

Flerit, F., R. Armijo, G. King, and B. Meyer (2004), The mechanical interaction between the propagating North Anatolian Fault and the back-arc extension in the Aegean, *Earth Planet. Sci. Lett.*, *224*, 347–362, doi:10.1016/j.epsl.2004.05.028.

Görür, N., and Ş. Elbek (2013), Tectonic events responsible for shaping the Sea of Marmara and its surrounding region, *Geodin. Acta*, (January), 1–11, doi:10.1080/09853111.2013.859346.

Gasperini, L., A. Polonia, M. N. Çağatay, G. Bortoluzzi, and V. Ferrante (2011a), Geological slip rates along the North Anatolian Fault in the Marmara region, *Tectonics*, *30*, 1–14, doi:10.1029/2011TC002906.

Gasperini, L., A. Polonia, G. Bortoluzzi, P. Henry, X. Le Pichon, M. Tryon, N. Çağatay, and L. Géli (2011b), How far did the surface rupture of the 1999 İzmit earthquake reach in Sea of Marmara?, Tectonics, 30, doi:10.1029/2010TC002726.

Grall, C., P. Henry, Y. Thomas, G. K. Westbrook, M. N. Çağatay, B. Marsset, H. Saritas, G. Çifçi, and L. Géli (2013), Slip rate estimation along the western segment of the main marmara fault over the last 405-490 ka by correlating mass transport deposits, *Tectonics*, *32*, 1587–1601, doi:10.1002/2012TC003255.

Grall, C., P. Henry, G. K. Westbrook, M. N. Çağatay, Y. Thomas, B. Marsset, D. Borschneck, G. Cifçi, and L. Géli (2014), Mass transport deposits periodicity related to glacial cycles and marine-macustrine transitions on a ponded basin of the Sea of Marmara (Turkey) over the last 500 ka, in *6th International Symposium on Submarine Mass Movements and Their Consequences*, vol. 37, pp. 595–603.

Hergert, T., and O. Heidbach (2010), Slip-rate variability and distributed deformation in the Marmara Sea fault system, *Nat. Geosci.*, *3*(2), 132–135, doi:10.1038/ngeo739.

Hergert, T., O. Heidbach, A. Bécel, and M. Laigle (2011), Geomechanical model of the Marmara Sea region-I. 3-D contemporary kinematics, *Geophys. J. Int.*, *185*, 1073–1089, doi:10.1111/j.1365-246X.2011.04991.x.

Hubert-Ferrari, A. (2002), Morphology, displacement, and slip rates along the North Anatolian Fault, Turkey, *J. Geophys. Res.*, *107*, doi:10.1029/2001JB000393.

Karabulut, H., J. Schmittbuhl, S. Özalaybey, O. Lengliné, A. Kömeç-Mutlu, V. Durand, M. Bouchon, G. Daniel, and M. P. Bouin (2011), Evolution of the seismicity in the eastern Marmara Sea a decade before and after the 17 August 1999 Izmit earthquake, *Tectonophysics*, *510*(1-2), 17–27, doi:10.1016/j.tecto.2011.07.009.

Kurt, H. et al. (2013), Steady late quaternary slip rate on the Cinarcik section of the North Anatolian fault near Istanbul, Turkey, *Geophys. Res. Lett.*, *40*(17), 4555–4559, doi:10.1002/grl.50882.

Le Pichon, X., C. Imren, C. Rangin, a. M. C. Şengör, and M. Siyako (2014), The South Marmara Fault, *Int. J. Earth Sci.*, *103*, 219–231, doi:10.1007/s00531-013-0950-0.

Le Pichon, X., N. Chamot-Roooke, C. Rangin, and A. M. C. Sengör (2003), The North Anatolian fault in the Sea of Marmara, J. Geophys. Res., 108, 2179, doi:10.1029/2002JB001862.

Meghraoui, M., M. E. Aksoy, H. S. Akyüz, M. Ferry, A. Dikbaş, and E. Altunel (2012), Paleoseismology of the North Anatolian Fault at Güzelköy (Ganos segment, Turkey): Size and recurrence time of earthquake ruptures west of the Sea of Marmara, *Geochemistry, Geophys. Geosystems*, *13*(4), 1–26, doi:10.1029/2011GC003960.

Polonia, A. et al. (2004), Holocene slip rate of the North Anatolian Fault beneath the Sea of Marmara, *Earth Planet. Sci. Lett.*, *227*, 411–426, doi:10.1016/j.epsl.2004.07.042.

Rangin, C., X. Le Pichon, E. Demirbag, and C. Imren (2004), Strain localization in the Sea of Marmara: Propagation of the North Anatolian Fault in a now inactive pull-apart, *Tectonics*, *23*, 1–18, doi:10.1029/2002TC001437.

Reilinger, R., S. McClusky, D. Paradissis, S. Ergintav, and P. Vernant (2010), Geodetic constraints on the tectonic evolution of the Aegean region and strain accumulation along the Hellenic subduction zone, *Tectonophysics*, *488*(1-4), 22–30, doi:10.1016/j.tecto.2009.05.027.

Reilinger, R. et al. (2006), GPS constraints on continental deformation in the Africa-Arabia-Eurasia continental collision zone and implications for the dynamics of plate interactions, *J. Geophys. Res. Solid Earth*, *111*, 1–26, doi:10.1029/2005JB004051.

Seeber, L., O. Emre, M. Cormier, C. C. Sorlien, and C. M. G. Mchugh (2004), Uplift and subsidence from oblique slip : the Ganos – Marmara bend of the North Anatolian Transform , Western Turkey, *Tectonophysics*, *391*, 239–258, doi:10.1016/j.tecto.2004.07.015.

Seeber, L., M. H. Cormier, C. McHugh, O. Emre, A. Polonia, and C. Sorlien (2006), Rapid subsidence and sedimentation from oblique slip near a bend on the North

Anatolian transform fault in the Marmara Sea, Turkey, *Geology*, *34*(February 2009), 933–936, doi:10.1130/G22520A.1.

Şengör, A. M. C., C. Grall, C. İmren, X. Le Pichon, N. Görür, P. Henry, H. Karabulut, and M. Siyako (2014), The geometry of the North Anatolian transform fault in the Sea of Marmara and its temporal evolution: implications for the development of intracontinental transform faults 1, *Can. J. Earth Sci.*, *51*(3), 222–242, doi:10.1139/cjes-2013-0160.

Sorlien, C. C. et al. (2012), Uniform basin growth over the last 500ka, North Anatolian Fault, Marmara Sea, Turkey, *Tectonophysics*, *518-521*, 1–16, doi:10.1016/j.tecto.2011.10.006.

Vidal, L., G. Ménot, C. Joly, H. Bruneton, F. Rostek, M. N. Çağatay, C. Major, and E. Bard (2010), Hydrology in the Sea of Marmara during the last 23 ka: Implications for timing of Black Sea connections and sapropel deposition, Paleoceanography, 25, 1–16, doi:10.1029/2009PA001735.

Zabcı, C., T. Sançar, H. S. Akyüz, and N. G. Kıyak (2015), Spatial slip behavior of large strike-slip fault belts: Implications for the Holocene slip rates of the eastern termination of the North Anatolian Fault, Turkey, *J. Geophys. Res. Solid Earth*, *120*(12), 8591–8609, doi:10.1002/2015JB011874.

Zitter, T. A. C., C. Grall, P. Henry, M. S. Özeren, M. N. Çağatay, a. M. C. Şengör, L. Gasperini, B. M. de Lépinay, and L. Géli (2012), Distribution, morphology and triggers of submarine mass wasting in the Sea of Marmara, Mar. Geol., 329-331, 58–74, doi:10.1016/j.margeo.2012.09.002.

ANNEX: Manuscript on crustal thinning in the Sea of Marmara

Moho depth and crustal thinning in the Marmara Sea region from gravity data inversion

J Kende[1], P Henry[1], G Bayrakci[2], S Ozeren[3], C. Grall[4]

[1]CEREGE, CNRS-Aix Marseille Université, Marseille, France

[2]National Oceanography Centre, University of Southampton, OES, United Kingdom

[3]İstanbul Teknik Üniversitesi, Maden Fakültesi, Jeoloji Bölümü, Ayazağa 34469 İstanbul TURKEY

[4]Lamont - Doherty Earth Observatory Columbia University, Marine Geology and Geophysics, New York City, USA

Corresponding author: Julia Kende (kende@cerege.fr)

Key Points:

- **Gravity data corrected from the sedimentary basins are inverted to build a Moho topography**
- **The 3D crust model obtained is used to compute the total extension in the area**
- **Results are compared with current extension rate**

Abstract

In zones where geophysical surveys give a partial knowledge of the lower crust characteristics, gravity inversion is a way to construct a 3D model of the Moho topography. We used reflection, refraction and tomography seismic studies to constrain an inversion of satellite and survey vessel gravity data in the Marmara Sea area. The inversion method presented is close to the Parker-Oldenburg method. The result is a Moho topography showing a crust thinning extending further than the limits of the Marmara Sea sediment basins. The minimum Moho depth observed is of about 25 km, 5 km above the reference depth we chose. We then used the model to evaluate the overall Neogene extension in the area through a crust volume calculation. Comparing this surface with extension rate from GPS data, we found a good compatibility indicating that a constant extension rate was probably maintained during a reorganization of the tectonic regime from the Marmara area system before the North Anatolian Fault incursion to the dominantly strike-slip current system. We also evaluated the amount of extension carried by ductile flow in the lower crust and found that only 1.5 km of NS extension along the 200 km long zone is needed to explain the geometry. Our main uncertainties are related to the densities characterizing our model. A range of realistic values was evaluated for the sediment basins but, as crust temperatures have been shown to increase southward under the Marmara Sea, lateral variations of the crust and mantle densities are likely.

1. Introduction

Basin formation along strike-slip fault zones generally results from crustal extension at a releasing bend or releasing overstep [e.g. *Christie-Blick and Biddle*, 1985; *Biddle and Christie-Blick*, 1985]. The rheology of the lower crust and the ratio of step width to brittle crust thickness thus appear as essential parameters controlling the distribution of extension, basin geometry and sediment thickness [*Petrunin et al.*, 2006; *Smit et al.*, 2008]. With this respect, the Dead Sea and the Death Valley have been considered as end member cases. The Dead Sea pull-apart corresponds to a small 10 km step-over in a mostly brittle 35 km crust, in which case the extension occurs along the basin axis and remains confined in the narrow corridor defined by the bounding strike-slip faults [*Katzman et al.*, 1995; *Petrunin et al.*, 2006; *Ten Brink et al.*, 1993]. The Death Valley fault corresponds to a more than 50 km step in a relatively thin brittle crust, in which case the basin developed as an oblique structure bounded by normal faults [*Burchfiel and Stewart*, 1966]. Remarkably, in both cases, the Moho is not uplifted beneath the basins, as crust-mantle decoupling occurred for contrasted reasons. The Dead Sea basin is essentially uncompensated, with little involvement of the mantle in the formation of the basin [*Ten Brink et al.*, 1993; *Petrunin et al.*, 2006]. Below the Death Valley the crust is hot and highly ductile, affected by the regional Basin and Range extension, resulting in compensation within the crust, and a flat Moho [*De Voogd et al.*, 1988; *Fliedner et al.*, 1996]. The Sea of Marmara corresponds to an intermediate case where the step width is comparable to the width of the brittle crust (15-20 km), as may be estimated from the depth distribution of earthquakes [*Karabulut et al.*, 2011], and wide-angle refraction studies indicate a Moho at 26 km depth below sea level beneath the Sea of Marmara troughs, implying at least 5 km of uplift [*Bécel et al.*, 2009]. The conditions prevailing in the Sea of Marmara area may in fact be more representative of strike-slip basins in continental crust worldwide than the Dead Sea and Death Valley end members, hence motivating the present study.

The Marmara Sea is situated along a segment of the North Anatolian Fault (NAF), a vast fault system carrying 20 to 27 mm/yr of dextral strike-slip motion, according to GPS, between the Anatolian and the Eurasian plates [*Reilinger et al.*, 2006; *Hergert and Heidbach*, 2010]. In its western part, the NAF splits into several branches. The Marmara Sea overlies the NAF northern branch, the Main Marmara Fault (MMF) [*Le Pichon et al.*, 2001, *Şengör et al.*, 2005] (see Figure 1). While the MMF is interpreted as a pure, or dominantly, strike-slip fault [e.g. *Rangin et al.*, 2004; *Seeber et al.*, 2004], there are remaining uncertainties about the amount of extension taken up in the Sea of Marmara region and about the extensional mechanisms that led to the present basin geometries. *Bécel et al.* [2009] interpreted a northward dipping seismic reflector as a detachment oriented N40°E south of the Central Basin and suggested an asymmetric crustal thinning towards the SW. In the same study, *Bécel et al.* [2009] identified Pn wave, refracted on top of the upper mantle, in wide-angle seismic data and showed that the crustal thinning spreads southward over broader domain than the deep basins composing the North Marmara Trough (NMT). This result has been confirmed by a north to south onshore seismic survey [*Karabulut et al.*, 2013], cutting the Sea of Marmara at about the Marmara Island longitude and showing a crust thinning from 30 to 25 km, spread over a zone wider than the Marmara Sea.

We here combine available constraints from seismic studies [*Bécel et al.*, 2009; *Karabulut et al.*, 2013; *Bayrakci et al.*, 2013] with gravity modeling to produce a Moho depth map, draw a budget of crustal extension, and evaluate the contribution of flow in the lower crust to crustal extension processes in this strike-slip basin.

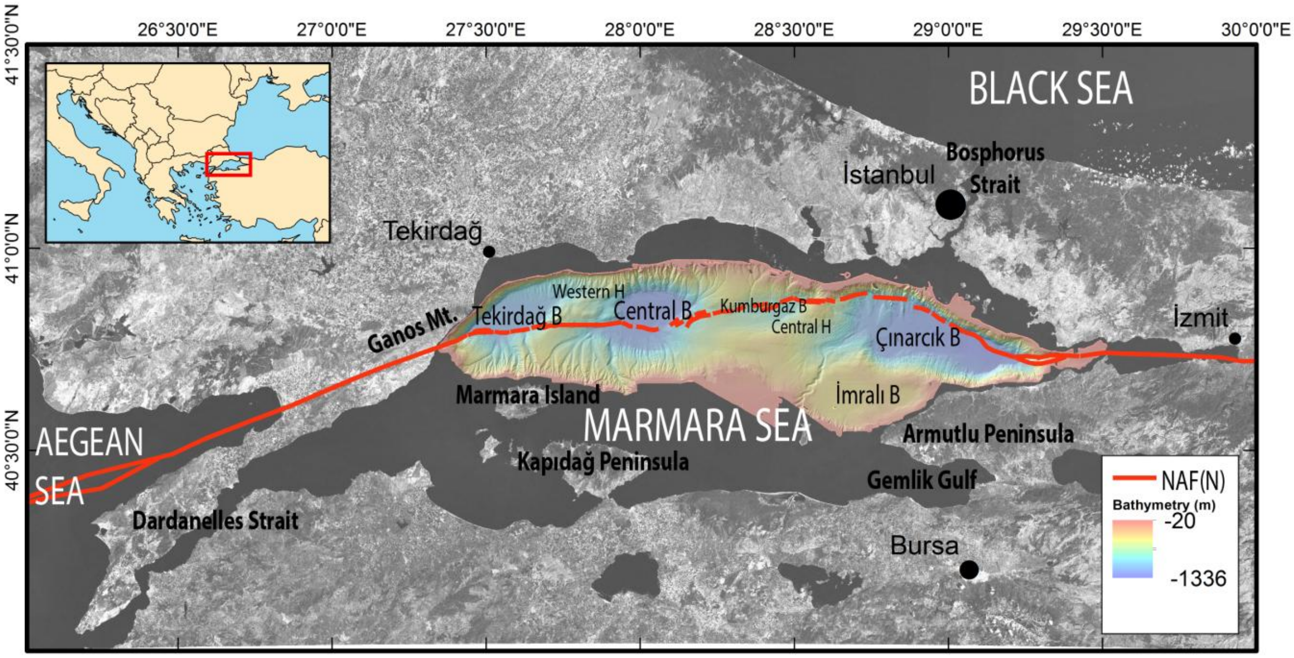

Figure 1. Geographic and simplified tectonic setting of the Marmara Sea. B stands for Basins, H for Highs and NAF(N) for the Northern branch of the North Anatolian Fault. The Fault location is modified from Şengör et al. [2014]. Bathymetry data are from the EM300 multibean survey.

2. Data

2.1. Gravity and topographic data

Two types of data were combined to build the gravity map used in our model.

First, we retrieved a global gravity grid from the Scripps Institution of Oceanography website. It provides marine gravity data from altimeter satellites [*Sandwell at al.*, 1997]. The altimetry of the sea surface is measured by combining the round trip travel time of pulses emitted from the satellite and the geodetic coordinates of the satellite computed from ground tracking [*Wahr*, 1996]. The result is a sea surface map, with attenuation of wave effects and local disturbances due to the radar pulse hitting the surface. A post-processing is then necessary to remove atmospheric propagation errors. The final data, available on http://topex.ucsd.edu/WWW_html/mar_grav.html, are based on past 3 to 4 mGal accurate Geosat and ERS-1 satellites data and includes new altimeter data from Envisat, CryoSat-2 and Jason-1 satellites. The data present a spatial resolution of about

7 km and have an estimated accuracy of 1.7 mGal at the Marmara Sea Latitude [*Sandwell et al.*, 2013]. A linear interpolation was used to refine the map in order to obtain a 256x512 cell grid covering the considered area and appropriate for fast Fourier transforms. The area of our study covers latitudes between 40° and 41.5° and longitudes between 26° and 30°.

The second data source is the gravity data collected during the Marsite Cruise in October and November 2014 on board the survey vessel NO Pourquoi Pas?. The ship is equipped with a Bodenseewerk KSS 31 gravimeter working with a spring on a stabilized platform. The device is installed at the ship steadiest spot and records data at a high time resolution giving a space resolution of about 1 m. As the measured free-air anomaly is relative, the mean value of the ship data was moved to match the satellite data mean value in the Marmara Sea. Then, a 256x512 cell grid covering our area of study was created from the ship data with linear interpolation and extrapolation from the closest value.

Figure 2. shows a comparison of the two data sources on a transect. Except on places where there is an obvious incompatibility between the two data sets, values are close and vary similarly. The shift observed in the west probably comes from the fact that the transect cuts an extremum in the satellite data. Thus, the spline interpolation overestimated the gravity from nearby trends.

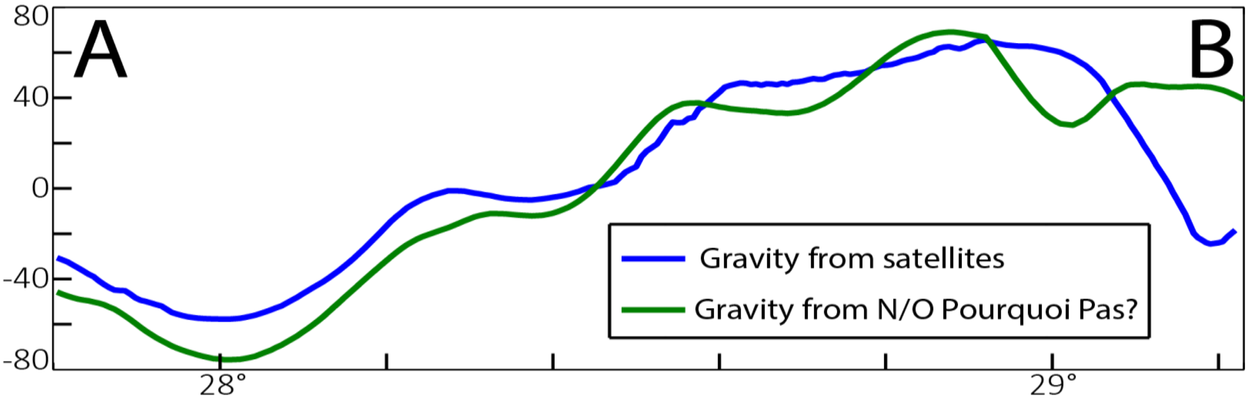

Figure 2. Comparison of the gravity data from satellites and from the gravimeter on board the N/O Pourquoi Pas? on a transect. Both data sets are interpolated and extrapolated if needed as no sections could exactly cut ship data and satellite data recording points. We chose a transect cutting zones that were crossed by the ship more than once. See transect location on Figure 3. The two data fields are centered on mean gravities calculated on the region where we have ship data.

The data were combined by using the grid created from ship data within 1700 m of the mission path and the grid from satellite data further than 4200 m. The corridors in between were filled through a biharmonic spline interpolation available in MATLAB and based on *Sandwell* [1987]. Figure 3 shows the gravity map before and after compiling the ship data with the satellite data. The merging delivered finer data in the Marmara Sea and eliminated an artefact in the East of the Marmara Sea (see Figure 3). However, as the mission path did not permit to record evenly spaced data over the study area, artefacts may remain in the final grid.

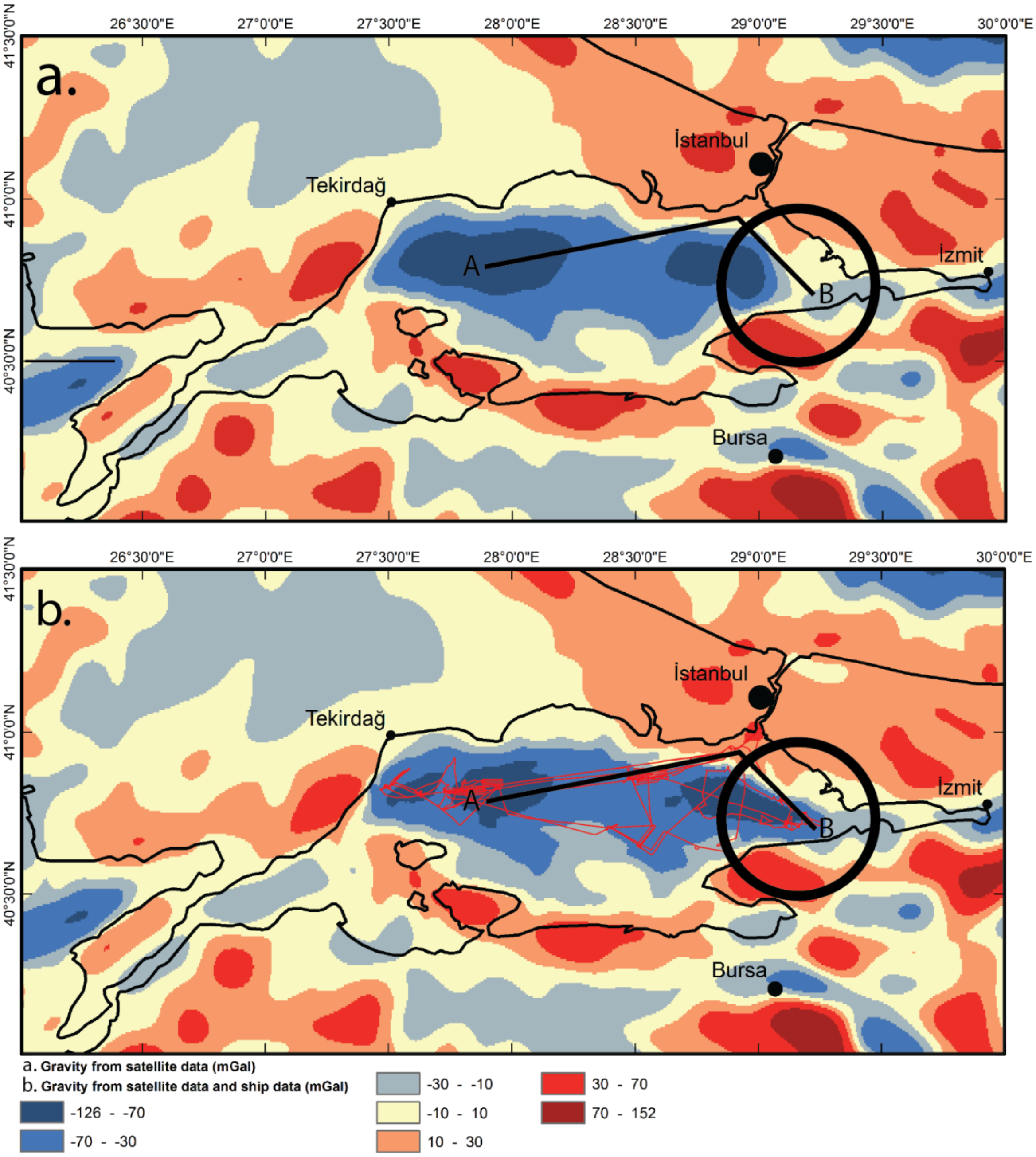

Figure 3. Gravity fields. a. Gravity field interpolated from satellite data only. b. Final gravity map combining the satellite data and the MARSITE cruise gravity measurement. Small onshore variations are due to the fact that both data sets are centered. Bold circle: location of the main artefact removed by integrating the ship data. Bold line: location of transect presented in Figure 2. Red fine line: N/O Pourquoi Pas? trajectory during the 2014 Marsite Cruise.

The bathymetry data used for the Marmara deep basins, presented in Figure 1, is based on the EM300 multibeam survey of the Sea of Marmara basins [*Le Pichon et al.*, 2001]. On the shelves and on land, the global topographic grid available from the Scripps Institution of Oceanography website was used.

2.2. Sediment thickness Data

The basin model used in this study is based on the sediment thicknesses derived from a tomographic study presented in *Bayrakci et al.* [2013]. This model was extended over the southern shelf based on TPAO multichannel seismic profiles interpretation [*Le Pichon et al.*, 2013]. The distinction made by *Bayrakci et al.* [2013] of a syn-kinematic layer and a pre-kinematic layer was adopted. For the locations where the model was expanded, the criterion discriminating the two layers was, when possible, the Vp velocity, as described in *Bayrakci et al.* [2013]. On the southern shelf, we chose the base of Neogene sediments as the syn-kinematic layer floor.

As the Moho will be modelled through low-frequency Fourier functions, the area governing the inversion results is not limited to the Marmara Sea. Nearby structures had to be modeled as well: the Black Sea and the Thrace Basin.

Only the southwestern part of the Black Sea was included in the domain of study. The sediment layers were extrapolated from the profile presented on Plate 14 in *Robinson et al.* [1996] by adopting a constant thickness of 600 m for the first as well as for the second layer of sediment. Thus, we obtain sediment depths directly related to the bathymetry. Although this is a rough approximation of the Black Sea complexity this approximation does not affect significantly our model in the Marmara Sea area.

The Thrace Basin sediment model was built based on *Siyako and Huvaz* [2007], *Hoşgörmez and Yalçın* [2005] and *Görür and Okay* [1996]. We ignored the Neogene sediments and constructed a coarse model of the Eocene-Oligocene basin interpolating between control points.

Finally, the two sediment depth maps were refined through a linear interpolation in order to obtain a 256x512 cell grid appropriate for fast Fourier transforms. Figure 4 shows the final thickness map for the two sediment layers.

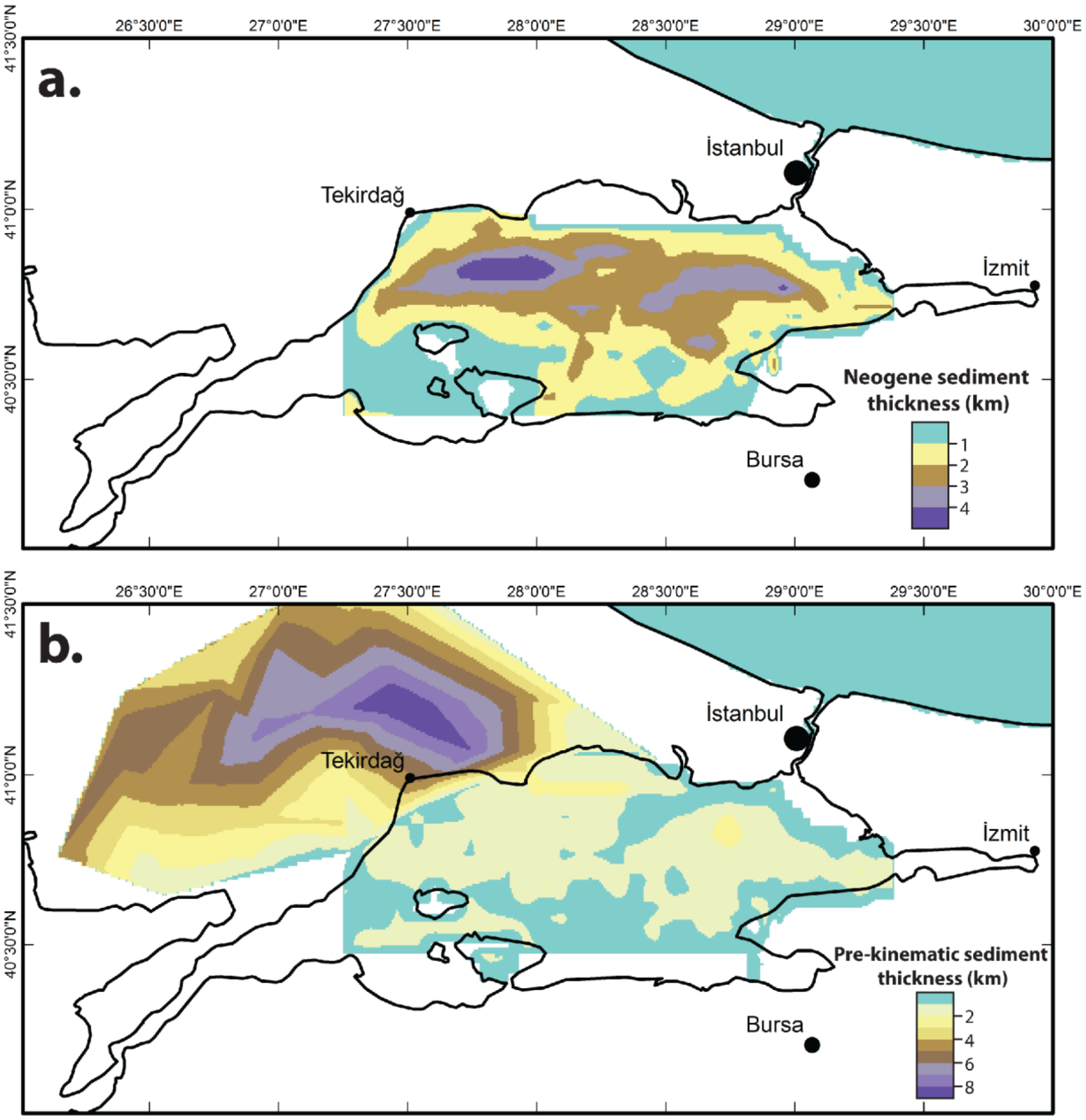

Figure 4. Thickness of the two sediment layers expended from Bayrakci et al. *[2013] model defined between 27.25° - 29.4° E and 40.5° - 41.1° N. The layers initial discrepancy is P-wave velocity variations. The Neogene sediments correspond to velocities lower than 4.2 km.s*$^{-1}$ *and the pre-kinematic sediments have Vp comprise between 4.2 km.s*$^{-1}$ *and 5.2 km.s*$^{-1}$. Bayrakci et al. *[2013] model was extended interpreting the bottom of the Neogene sediments as the interface between the two layers when P-wave velocities were not available. Neogene sediments are neglected in the Thrace Basin*

and a simple model with constant thickness characterizes the Black Sea.

3. Method

Modelling the Moho depth variations from gravity data is a two-step process. First, the gravity alteration resulting from the known geology and topography must be accounted for and removed from the observed gravity. The resulting gravity anomaly represent the outcome of deep density variations. We assumed that the remaining anomalies are directly related to Moho depth and can be inverted to determine the Moho depth variations.

For the first step, we decomposed the area in two domains and computed the effect of our upper-crust model on gravity through two different calculations:

3.1. Gravity correction in onshore domain

For the onshore domain, we simply applied a Bouguer correction which subtract, from the measured gravity, the variations induced by the topography. In the Thrace basin, we used a sediment density for the Bouguer calculation equal to the density of the pre-kinematic sediment layer.

Prior to computing the Bouguer correction, a Gaussian filter with a 20 km window was applied on the topography. This filtering was needed because wavelengths shorter than 20 km are absent from the gravity grid. This filtering does create a risk of interfering with crustal effect on gravity and loosing part of the signal [*Aitken et al.*, 2013].

3.2. Gravity correction in the Sea of Marmara, in the Black Sea and in the Thrace Basin

The Bouguer correction is a fast and effective approximation of the gravity anomaly caused by topography on land. But, as we need to account for the effect of the Sea of Marmara basins, the gravity must be corrected from the influence of the bathymetry variations and from the effect of water and sediment layers:

$$g_{corrected} = g_{measured} - \delta g_w - \delta g_{S_1} - \delta g_{S_2}$$

Where δg_w, δg_{S_1}, and δg_{S_2} are the effect on gravity of, respectively, the layer of water, the syn-kinematic sediments and the pre-kinematic sediments.

The basin correction was performed through the application of the Parker method [*Parker*, 1972], which is based on a Fourier transform of the gravity equation:

$$F[g(x)] = -2\pi G \Delta\rho e^{-|k|z_0} \sum_{n=1}^{\infty} \frac{|k|^{n-1}}{n!} F[h^n(x)] \qquad (1)\ Parker\ equation$$

Where $\Delta\rho$ is the density difference at the considered interface, k is the wavenumber of the transform function and z_0 is the mean depth of the considered interface. $F[g(x)]$ and $F[h^n(x)]$ are respectively the Fourier transform of the gravity field and of the interface depth.

The application of this method in the Marmara Sea is a three step process as we successively consider the water/syn-kinematic sediment interface, the syn-kinematic/ pre-kinematic sediment interface and the pre-kinematic sediment/Crust interface. Thus, $\Delta\rho$ is successively set as the density contrast at each interface. We obtain the gravity correction to be applied on the observed gravity field to account for any differences between our model and an ideal model with a flat topography and no sedimentary basins.

In the Thrace Basin, we have the particular case of a sedimentary basin with a positive topography. The Bouguer correction accounted for the positive topography and the Parker method accounted for the sedimentary basin below sea level.

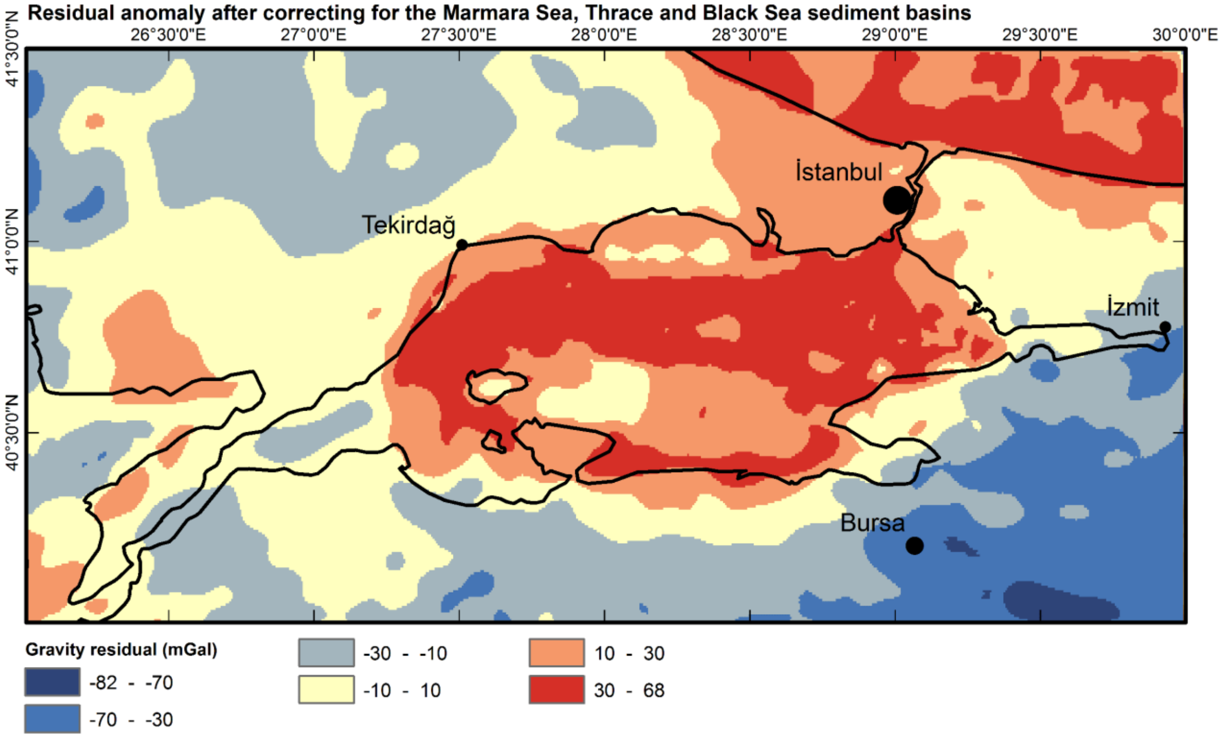

*Figure 5. Gravity anomaly after correcting the measured gravity field using Bouguer calculation for the topography and the Parker method [*Parker*, 1972] for the sediment basins.*

3.3. Residual anomaly inversion and Moho depth variation determination

Methods for determining the Moho variations and crustal thickness from gravity data have been used for more than a century [e.g. *Vening Meinesz*, 1931]. Approaches include inversion, forward-modeling, process-oriented modeling and spectral analysis (see *Aitken et al.* [2013] for a review).

Here, we developed a fast inversion method, close to the Parker-Oldenburg algorithm [*Oldenburg*, 1974]. First, the Parker equation was linearized, retaining only the first term of the Taylor development:

$$F[g(x)] = -2\pi G\Delta\rho e^{-|k|z_0} F[h(x)] \qquad (2)$$

This equation direct inversion is:

$$F[h(x)] = -\frac{e^{|k|z_0}}{2\pi G\Delta\rho} F[g(x)] \qquad (3)$$

This equation would not yield satisfactory results for the Moho because the high wave number terms are amplified while in fact they are unconstrained by data at wavelengths shorter than the crustal thickness. The method we propose is preconditioning to 0 the amplitude of Moho variations. A Least Square misfit function is thus defined, in the Fourrier domain as:

$$S[h] = \frac{1}{2\pi G\Delta\rho} \|F[g](k) - F[g_{obs}](k)\|^2 + \left\|\frac{F[h](k)}{\sqrt{C(k)}}\right\|^2 (4)$$

Where the covariance diagonal matrix C(k) scales the model deviation from the *a priori* model (flat Moho) with the error on data projected in the model space [*Tarantola*, 2005]. We will assume C(k) constant, independent of wavenumber. At short wavelengths, the first term is nearly independent of the model, and, at the minimum of S, h(k) ≈ 0. For long wavelengths, the first term becomes dominant, and the preconditioning has little effect on inversion results. The solution of this linear Least Square Problem is [*Tarantola*, 2005]:

$$F[h(x)] = \frac{1}{2\pi G\Delta\rho}\left(e^{-|k|z_0} \times e^{-|k|z_0} + \frac{1}{covar}\right)^{-1} \times e^{-|k|z_0} \times F[g_{obs}(x)] \qquad (5)$$

This is equivalent to applying a low pass filter to the linearly inverted Moho, where C controls the cut-off wavelength. One theoretical advantage of this method is that the shape of the filter is consistent with a preconditioning approach [*Tarantola*, 2005].

3.4. Process enhancement with an iterative loop

After computing a first Moho depth map by inverting the residual gravity anomaly, the geologic model was refined by adding an upper crust/lower crust boundary calculated proportionally from the Moho depth to be about 10 km above it [*Bécel et al.*, 2009]. Then, we computed a new residual anomaly, considering now five layers above the Moho: the water, the two sediment layers and the upper and lower crust with densities of, respectively, 2.65 and 2.95 g.cm^{-3}. From this new residual anomaly map, a new inversion was processed to define a new Moho depth map. This process is convergent and, repeated ten times, lowers the standard deviation of the final residual anomaly in the domain of study of about 0.7 mGal.

3.5. Modelling parameters

Using an inverse modelling method is a fast, effective and repeatable way to compute a model on a large area with a fine gridding. It also removes part of human biases that are a risk when carrying forward modelling in which the model is manually modified until it fits a set of conditions that describe an acceptable Moho and meets the geophysical observations [*Aitken et al.*, 2013]. However, the whole model is based on the acceptance of the initial shallow geologic setting, on the precision of the topographic and gravimetric surveys and on the few parameters that are user-input: the layer densities, the reference Moho depth and the covariance parameter for the Moho inversion.

The geologic model we first used consisted of five layers, each characterized by a density: water, first sediment layer (syn-kinematic), second sediment layer (pre-kinematic), crust and mantle.

The crust and mantle density were chosen based on *Bécel et al.* [2009] P-wave velocities and on *Sobolev and Babeyko* [1994] P-wave velocity versus density curves. Thus we selected 2.75 g.cm^{-3} for the crust: we considered two third of upper crust with Vp between 6 and 6.2 km.s^{-1} and a third of lower crust with Vp = 6.7 km.s^{-1}, corresponding respectively to 2.6, 2.7 and 2.95 g.cm^{-3} [*Sobolev and Babeyko*, 1994]. Mantle density is taken equal to 3.33 g.cm^{-3}.

Estimating valid mean densities for the sedimentary basins is less straight-forward as there is no simple general relationship between density and velocity for sediments. *Bayrakci et al.* [2013] defined the two layers with P-wave iso-velocity contours: the first layer refers to the field in which P-wave velocity is smaller than 4.2 km.s^{-1} whereas pre-kinematic sediments are defined between 4.2 km.s^{-1} and 5.2 km.s^{-1}. To evaluate the density at the level of the 4.2 km.s^{-1} iso-velocity contour, we used a relationship for siliciclastic sediments from *Erickson and Jarrard* [1998] to deduce a maximum and a minimum density value:

$$V_p = 1.11 + 1.178\emptyset + \frac{0.305}{[(\emptyset + 0.135)^2 + 0.0725]} + 0.61(v_{sh} - 1)(X - abs(X))$$

Where $X = \tanh\big(20(\emptyset - 0.39)\big)$. V_p is the compressional wave velocity, v_{sh} the shale fraction and $\emptyset$ the porosity. As sediments may change from very fine clay to continental coarser layers, we tested the relation with v_{sh} varying from 0 to 1. We obtained the limit values of 2.40 g.cm^{-3} ($\emptyset = 0.15$) and 2.63 g.cm^{-3} ($\emptyset = 0.01$), using 2.65 for siliciclastic grain density. One should note that the value calculated with $v_{sh} = 1$ largely encompass the possible drifting described by Erickson and Jarrard [1998] when dealing with very low porosities. Then, considering a porosity for shallow clay rich sediments of 0.7 [*Le Pichon et al*., 1990], which is consistent with measurements on Sea of Marmara sediment cores [*Aloisi et al*., 2015], and an exponential porosity-depth law (Athy's law, [*Grall et al*., 2012 and 2013]) from the sediment layer top to its floor, we obtain a range of 2.07 to 2.39 g.cm^{-3} for the average density of the first layer of sediment.

For the bottom limit of the second layer, we used the same equation and $v_{sh} = 0$ $v_{sh} = 0$to determine a minimum density of 2.60 g.cm^{-3} ($\emptyset = 0.03$)$\emptyset = 0.03$). From this value and the one calculated at the layer top, we get an average minimum density for the second layer of sediment of 2.53 g.cm^{-3} ($\emptyset = 0.07$$\emptyset = 0.07$). We then consider 2.65g.cm^{-3} as a maximum.

The two ranges of density were scanned with a step of 0.02 g.cm^{-3} and all combinations were tested. Each time, we calculated the residual gravity after correcting for the Marmara Sea Basins without taking into account the Thrace Basin and the Black Sea sediments.

The comparison of the residual standard deviations indicates that the higher the density values are, the smaller the residual gravity anomaly is. This result is understandable, as the correction for basin topography is comparable in amplitude to the initially negative free air anomaly. Taking into account that sediment density is lower than average crustal density results in a positive anomaly which amplitude depends on the assumed sedimentary layer densities. We assume that this residual anomaly could, in great part, be explained by variations of crustal thickness.

In the following parts of this article, the discussion will be based on a model obtained with the mean values of 2.23 and 2.59 g.cm^{-3}. We will also consider that varying the density within the determined range yields the possible range of variation of Moho depth maps as constrained by gravity.

For the inversion of the corrected gravity field, two parameters have to be set: the mean Moho depth and the covariance.

The choice of the mean Moho depth was based on *Karabulut et al*. [2013] and set to 30 km. We preferred that value to the about 35 km depth inferred around the Marmara Sea in *Bécel et al.* [2009] as their distribution of receiver and sources does not constrain well the Moho depth outside the basins. It is also the reference value chosen by *Tiberi et al.* [2001] for their inversion of gravity data after correcting for the plunging African slab in the Corinth Rift area.

The covariance parameter has a direct impact on the Moho results. We tested covariance ranging from 1/10 to 1/50 and selected 1/25 as it gives the depth variation amplitude closest to the one observed by *Karabulut et al.* [2013].

4. Results

Figure 6 shows the Moho depth and the final residual, which is the difference between the measured gravity and the modeled gravity. Results computed with the minimum and maximum sediment densities within the bounds we defined are also presented. One should note that, although the Moho depth variation amplitude changes, the geometry is similar on all three results. We observe a thinning spread further North than South of the Marmara Sea considering 30 km depth as the default depth in a homogenous crust and two shallowest zone, north of the Marmara Island and in the Cinarcik Basin.

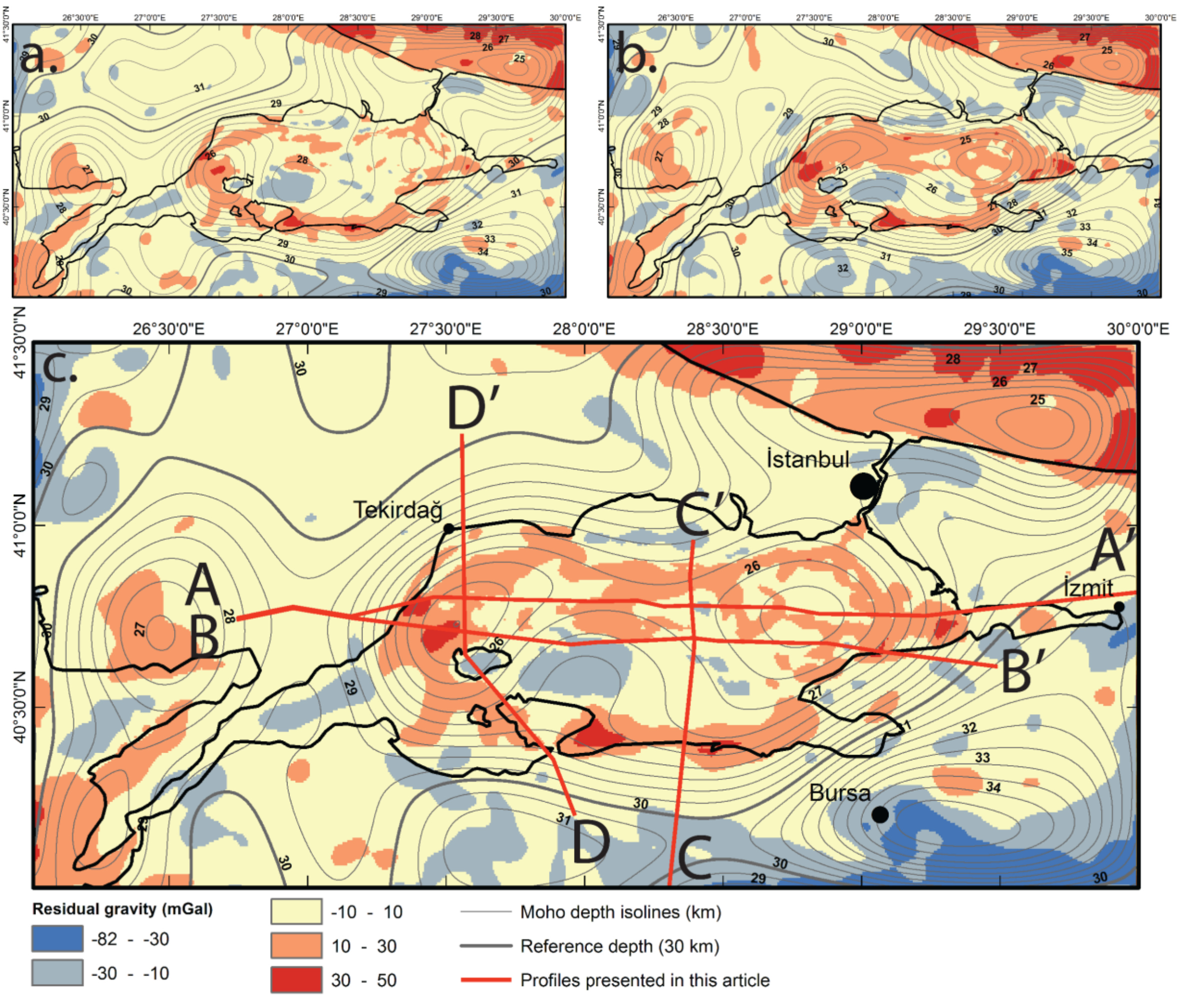

Figure 6. Moho depth topography and gravity residual computed with variable density for the syn-kinematic sediment layer and the pre-kynematic sediment layer with, respectively: a. 2.07 and 2.53 g.cm-^{3}, b. 2.39 and 2.65 g.cm-^{3} and c. 2.23 and 2.59 g.cm-^{3}. Thick red lines: locations of profiles presented in Figure 7.

The modeled gravity is the summation of on land Bouguer correction, basin effects on the gravity and the gravity anomaly produced by the inferred Moho and upper crust/lower crust boundary. Thus, observation of the gravity residual is representative of the model accuracy as it is the part of the gravity measurement not explained by our model.

As presented in Figure 6, with each of the sediment density pair inputs, we obtain a map with a residual gravity anomaly equal to 0 ± 10 mGal on the majority of our domain of study.

In the Marmara Sea, the residual is characterized by a positive “belt” spreading from East to West above the basins and along the southern shore. In the middle, the Marmara Island, the zone North of the Kapıdağ Peninsula and the Imrali Basin, are small areas with negative residuals. We will discuss separately the northern and the southern part of the positive “belt” as they probably result from two different mechanisms.

The northern part of the “belt” coincides with the deep basins and show the highest residuals at the location of the current depocenters in the Imrali and the Cinarcik basins. This may be due to the fact that sediment layers are characterized by only one mean density, which may be too small for zones with a very thick sediment layer. Similarly, as the residual above the basins is decreased by highest density values, the density ranges we defined earlier may be overly shifted toward lower density values. Also, in this zone, the positive residual creates a pattern which coincides with the MARSITE mission ship path. Thus, although the merging of the Pourquoi Pas? and the satellite data was necessary to suppress a large artefact in the east (see Figure 3), the two data source may not be coherent enough. We could probably lower this positive residual by normalizing the ship data in regards of the satellite data, instead of only matching the averages. But the area covered by the ship data may not be wide enough to be representative and to allow such a correction. The positive residual is also probably due to the fact that short wavelength information are not corrected by the model. So short wavelength gravity variations are still visible only where they were recorded: along the ship path.

The southern part of the positive “belt”, which spreads along the southern shore, coincides with a positive gravity anomaly in the initial gravity data (see Figure 3). The preservation of this positive anomaly as a residual, independently of the sediment densities, indicates that our model probably lacks a structure which should account for it. The shape of this anomaly may also evocate an elastic flexure effect which is not considered in our model. However, the scale and the position of this anomaly, in the middle of the zone of crustal thinning gradient, makes this hypothesis questionable. Away from the Marmara Sea, at the limits of the area of study in the North-East and South-East directions, the overly bended Moho indicates an edge effect due to the fact that the Moho is approximated with Fourier transforms. This problem will not be discussed further as the area is large enough to avoid such effect near the Marmara Sea.

4.1. Compatibility with consulted geophysical studies

To assess the accuracy of our model, we here compare our results with previously published Moho depth data from geophysical surveys: *Bécel et al*. [2009] profiles based on Multi-Channel reflection Seismic (MCS) lines, on-land stations and OBSs, and *Karabulut et al.* [2013] high scale North-South profile based on a tomographic study. As the parameters in our study were chosen in order to reach a model close to those constructed by these geophysical surveys, it is expected that amplitude and main structures are alike. We will discuss the remaining differences.

In *Bécel et al.* [2009], three profiles based on marine multi-channel reflection seismic, Ocean Bottom Seismometers (OBSs) and onshore reflection/refraction records are presented. Figure 7 shows a comparison of these three profiles and of our results.

The AA' *Bécel et al.* [2009] profile under the MMT shows a thinning almost constant under the main basins and a rapid return to a depth of about 35 km around the Marmara Sea. Because of the thick layer of sediments, only OBSs and on land station gave constraints on the Moho depth. Our 3D model is coherent with this 2D model under the basins, with a Moho depth at about 25 km and a slightly thicker crust in the central part of the Sea of Marmara. Away from the basins, the thinning is less spread on *Bécel et al.* [2009] model. This could be explained by less constraints away from the basins since only the wide angle refraction toward the sparse land stations gave some data.

The coherency of the two models along the southern shelf E-W BB' is more questionable as *Bécel et al.* [2009] show a thinning under the limits of the Imrali Basin whereas our model gives a similar result as the profile under the MMT with a wider bending slightly displaced to the west, centered approximately south of the Central Basin. However, the main data used to constrain this southern profile by *Bécel et al.* [2009] are shots along a MCS line which was limited to the ship trajectory East of Marmara Island. On the western extremity of this line, *Bécel* [2006] detected evidence of a deepening of the lower crust top. This could correspond to the edge of the thinning centered, in our model, in the Imrali Basin. Moreover, the lower crust/upper crust limit may not follow exactly the Moho variation. The western part of *Bécel et al.* [2009] southern profile was derived solely from on land stations and extrapolation of the MSC East profile. Consequently, they may lack evidence for another thinned zone, visible on our model, which corresponds to the edge of the depression centered north of the Marmara Island.

The third interpreted profile CC' by *Bécel et al.* [2009] is oriented NS and shows that a thinning under the North Marmara Trough is required in order to fit the computed PmP waves travel time with records from the Oren on land station in the south. The profile in our model present a shallower Moho overall but the inclination inferred from the Oren station of 4.3° is very close to the inclination in our model, at the location of Bécel's constraint on the Moho.

All in all, our model is quite consistent with *Bécel et al.* [2009]. But with their data set, *Bécel et al.* [2009], could only identify the thinning under the main basins: the MMT and the Imrali Basin. We show that the thinning zone is wider and extends southward, including below the anticlinal fold region of Marmara Island [*Le Pichon et al.*, 2013].

The 650 km long profile presented in *Karabulut et al.* [2013] was constructed by a tomography study using receiver functions. Data from a selection of 60 seismic events were recorded by both permanent and temporary stations installed along the profile axis, forming a network with an inner spacing of about 15 km. As only on land stations were used, the data spacing is not as tight in the Marmara Sea. Furthermore, *Karabulut et al.* [2013] had gaps of about 65 km in the north and 30 km in the south between the stations along the shores and the next stations on the profile. As our model amplitude in profile DD' was mainly based on *Karabulut et al.* [2013] study, we do observe the same depth in the middle of the Marmara Sea and away from the basins. However, the apparent wavelength of our model is different with a thinning spread on about 130 km compared to 220 km in *Karabulut et al.* [2013] model. As they were limited by the low number of station around the Marmara Sea, and as their horizontal resolution is about 40 km, our model is not incoherent with their data.

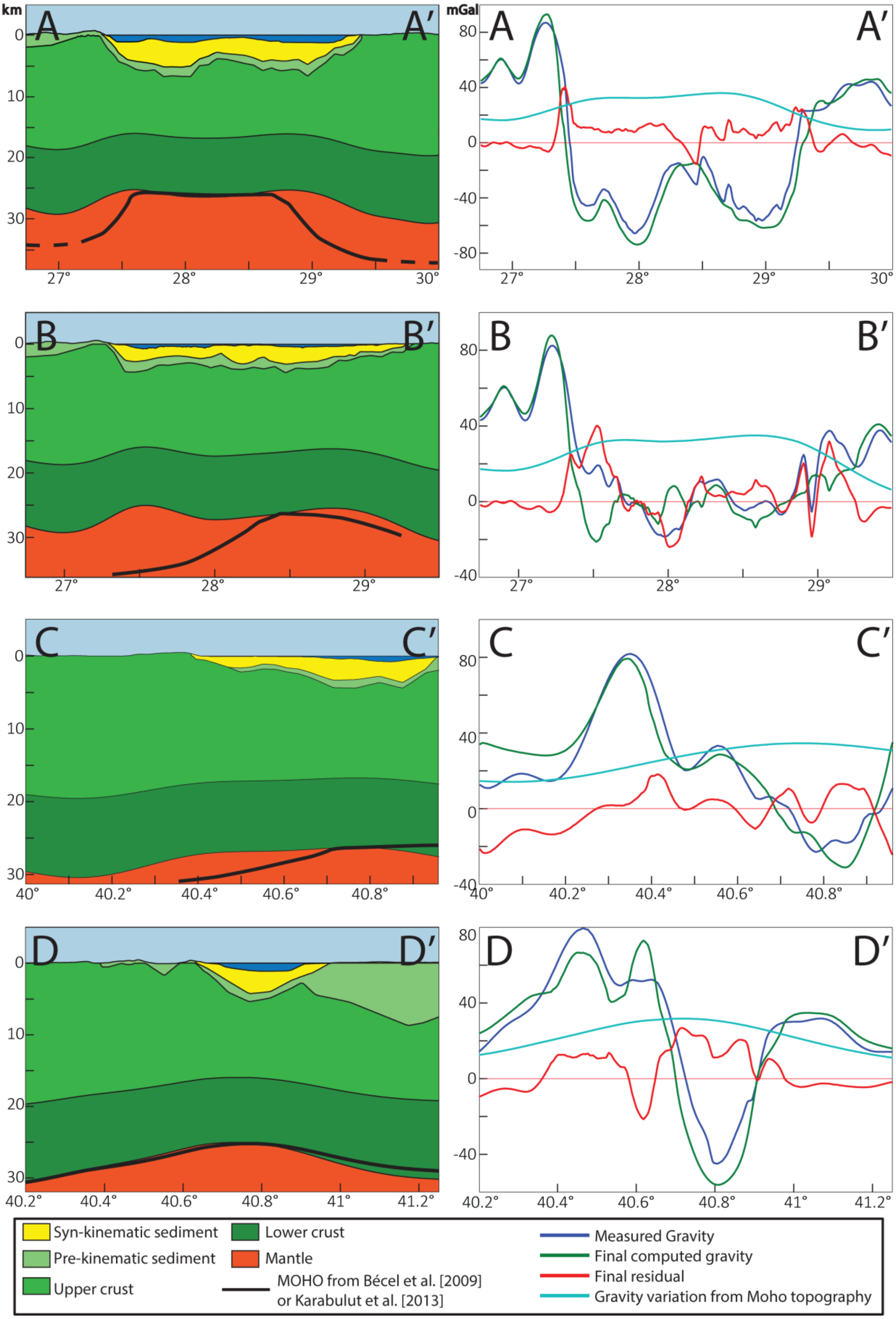
km
mGal
A
A′
B
B′
C
C′
D
D′
0
10
20
30
80
40
0
-40
-80
27°
28°
29°
30°
40°
40.2°
40.4°
40.6°
40.8°
41°
41.2°
Syn-kinematic sediment
Pre-kinematic sediment
Upper crust
Lower crust
Mantle
MOHO from Bécel et al. [2009] or Karabulut et al. [2013]
Measured Gravity
Final computed gravity
Final residual
Gravity variation from Moho topography

Figure 7. Gravity, geological data and results along four profiles (see location on Figure 6.c.). Left column: geological setting, modeled Moho and modeled upper crust/lower crust boundary. Right column: gravity measurement, computed gravity, residual anomaly and gravity field induced by Moho depth variation. Profiles A., B., and C. coincides with profiles presented in Bécel et al. [2009] and profiles D. is localized on Karabut et al. [2013] cross-section. Bold black lines on the left column represent Bécel et al. [2009] Moho depth on profiles A., B., and C., and Karabulut et al. [2013] Moho depth on profile D..

4.2. Comparison with other models

We compared our result with the MATLAB 3DINVER application of the Parker-Oldenbury method [*Gomez-Ortiz and Agarwal*, 2005].

The Parker-Oldengurg method, as computed in the 3Dinver algorithm by *Gomez-Ortiz and Agarwal* [2005], is also based on Parker's equation. First, gravity anomalies from the known geology are removed with the Parker method, as we did here. Then, the Parker equation is re-arranged and the first order is used to determine a first approximation of the Moho topography, before increasing the orders in a recursive process. At each step, the current Moho topography is filtered using a high-pass filter.

$$F\big(h_0(x)\big) = -\frac{F[\Delta g(x)]e^{(-kz_0)}}{2\pi G\rho}$$

$$F\big[h_{nf}(x)\big] = F[h_n(x)] * filter$$

$$F[h_{n+1}(x)] = -\frac{F[\Delta g(x)]e^{(-kz_0)}}{2\pi G\rho} - \sum_{i=1}^{n+1} \frac{k^i}{(i+1)!} F[{h_{nf}}^{i+1}(x)]$$

Using this method, we computed a Moho interface with varying filter parameters. We then looked for the solution with a frequency signature as close as possible to the frequency signature of our result by comparing the correlation coefficient of the two Fourier Transforms. We discarded a 20 km width outline at the edge of the area to avoid interferences from edge effects. The best result gives a correlation coefficient of 0,998. As shown in Figure 8, the results are very similar. However, the 3Dinver solution shows variations with higher amplitude and a thinning with a less pronounced asymmetry. As for the quantitative assessment of the two results, our model gives a standard deviation for the residual gravity of about 3.62 mGal before the looped post-processing and 2.93

mGal after, compared to 4.13 mGal for the 3Dinver solution which, is, again, close to our result.

To evaluate further the acceptability of our model, we compared it to an isostatic filtered model.

The isostatic Moho model was calculated through an Airy mass compensation condition on columns of 35 km thickness and of about 0.4 km^2. The compensation was made to fit with an ideal column of 30 km of crust and 5 km of mantle. The basin model is the same as before, with two sediments layers. The resulting Moho was filtered through a Butterworth low-pass filter with a cutoff wavelength of about 90 km and a high order. This filter parameter corresponds to the best value for comparing with the Moho calculated by inversion methods, which are low-passed by construction.

The result (see Figure 8.b) is close to the Moho inverted from gravity values, with two areas of maximum thinning in the Eastern and Western parts of the Sea of Mamara. Also, the western zone of thinning in the isostatic model is centered NE of the Marmara Island, not North of the island. This result is unsurprising as, by construction, the isostatically compensated Moho image is merely a filtered image of the basin geometry. The maximum thinning zones thus correspond to the areas with the highest thicknesses of basin fill. The range of Moho depth variations is also comparable, which indicates that the present day basin geometry is in large part isostatically compensated.

The residual gravity anomaly of the isostatic model (difference between measured gravity and isostatic model gravity anomaly) is related to the local isostatic unbalance. The western part of the Sea of Marmara and the Thrace Basin seem to have a mass deficit, while the peripheric region appears positive. This could in part results from flexural response around the basins. However, the positive residual along the southern shore of the Sea of Marmara is too narrow to be explained by lithospheric flexural bending [eg: *Watts et al.*, 1982; *Watts and Burov*, 2003; *Zuber et al.*, 1989]. This more likely reflects crustal scale structures and, possibly, flexural response at the scale of crustal tilted blocks. At large wavelengths, the difference observed between the eastern and western Sea of Marmara is also puzzling and suggests that an uncompensated lithospheric anomaly extending beneath the Thrace Basin and Western Sea of Marmara, and not related to NAF tectonics, may influence the gravity field.

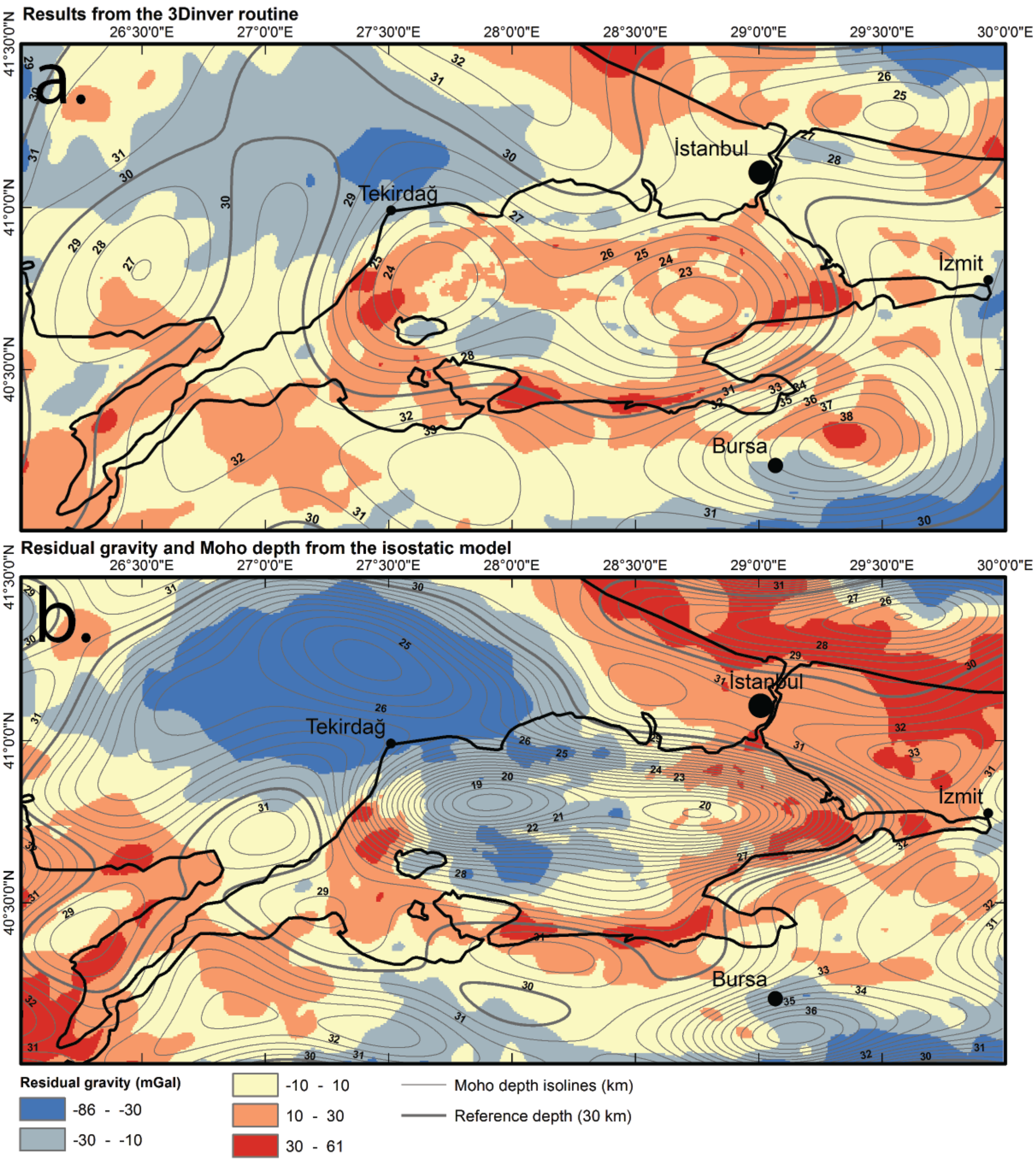

Figure 8. Gravity residual and Moho depth obtained with the 3DINVER program [Gomez-Ortiz and Agarwal, 2005] and an isostatic model. Geological setting, gravity data and sediment characteristics used as inputs are the same as in previous models. a. Results with the 3DINVER program. Parameters specific to this routine were chosen in order to obtain a Moho topography with a frequency signature close to our result. b. Results with an isostatic model. The Moho topography is filtered from calculation with a compensation depth set at 35 km and a reference crust of 30 km thickness. It is a direct response to the geological model.

5. Discussion and conclusion

The Moho depth variation model computed in this study shows a distribution of thinning which appears to roughly mimic the base of the syntectonic basins [*Bayrakci et al.*, 2013]. The Moho highs do not exactly match the crustal lows but are both close to the two Marmara most active basins. The two highs are separated by an inflexion in the Moho roughly at the Central High location, where the minimum extension is observed in the North Marmara Trough. The thinning also appears to spread over a wider zone. This indicates that the stretching component of strain in the Sea of Marmara has been distributed differently in the upper crust and at the Moho level, implying some ductile flow in the lower crust.

If this model is hardly compatible with any model based on rigid blocks like *Armijo et al.* [1999] block model based on present day active fault geometry in the brittle crust, it shows a geometric compatibility with the low angle detachment system identified in the Eastern and Central Sea of Marmara from seismic reflexion and refraction profiles [*Bécel et al.*, 2010]. But the zone of crustal thinning still appears broader extending below the southern shelf and the Marmara Island. A more detailed comparison of the Moho topography and of the basement topography is presented in *Le Pichon et al.* [In Press].

5.1. Overall extension in the Marmara Sea

To quantify the overall extension accommodated during the Marmara Sea basins formation, we considered the volume difference between the crust in our model and a reference model with a constant 30 km thick crust and no sediment basins nor hills. Here, the term “crust”, refers to the lower and upper crust, as well as to the pre-kinematic sediment. In order to avoid interferences from older geological systems, we discarded zones where the Moho depth variations are influenced by Pre-Pliocene tectonics, for instance the Uludağ massif which exhumation occurred during the early Miocene [*Okay et al.*, 2008], the Black Sea, and the Thrace Basin. Figure 9 shows the final 19150 km^2 area we considered. We computed the proportion of the area that could be accommodated with this ideal crust, given the volume of crust in our model. We obtained that, with the volume of crust given by our model in the 19150 km^2 area we defined, a 30 km thick reference crust could cover only 17050±300 km^2. Thus, our model indicates a total of 2100±300 km^2 of extension during the formation of the Marmara Sea. The uncertainty is obtained by varying the sediment densities within the defined bounds and varying the reference Moho depth of 2 km around the 30 km reference value as it is *Karabulut et al.*

[2013] estimated uncertainty on Moho picks. Because the reference thickness is also an input for the Moho topography inversion, the uncertainty on “missing” surface may seem smaller than expected.

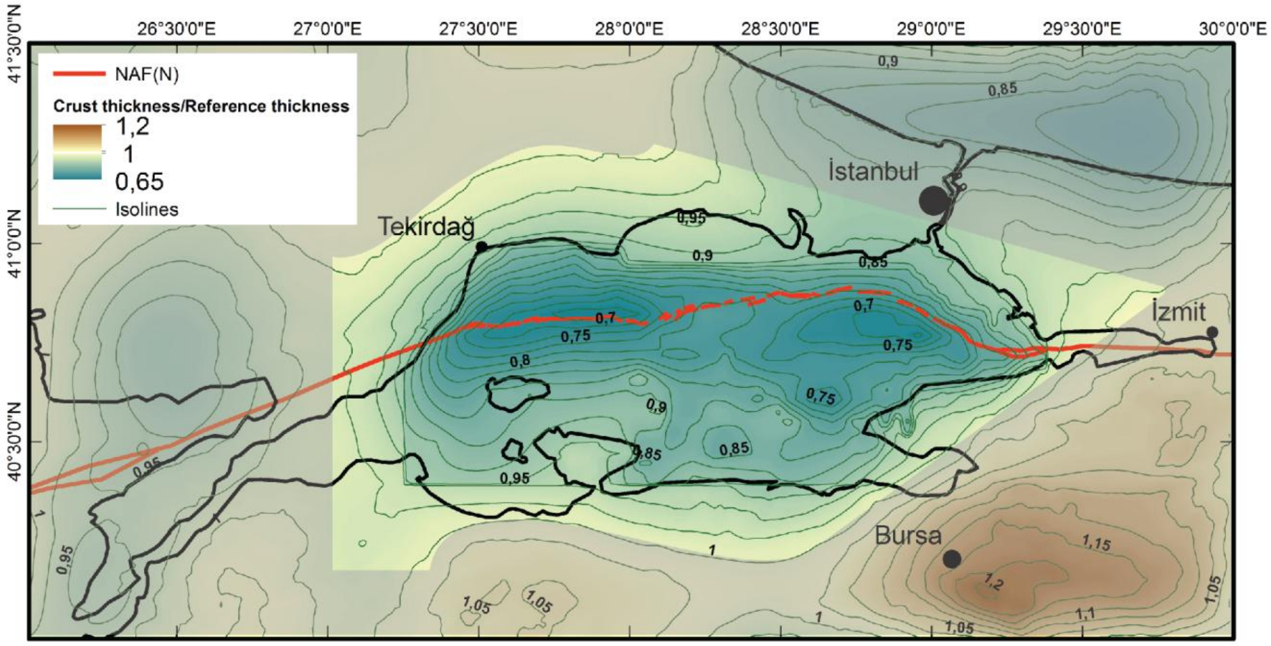

Figure 9. Thinning rate corresponding to our model crust thickness over 30 km reference thickness. The unshaded area correspond to the zone that was considered in a crust volume calculation to estimate a 2100±250 km^2 extension surface in the Marmara Sea. The rest of the area was set aside as we considered that the Moho topography below was controlled by pre-Neogene events.

Armijo et al. [2002] presented a reconstitution of the area at -5 Myr based on present day active fault geometry in the brittle crust. They delimited four rigid blocks creating two main zones where oblique slip and extension occur, above the deep basins and on the southern shelf margin. A third zone, further south, will not be considered as it is in great part outside of the area we modeled. Between these two systems, an additional fault system identified beneath the Southern continental shelf, the Southern Marmara Fault, has been mostly active during the Pliocene [*Le Pichon et al.*, 2012]. The total slip on the Shelf Fault is not precisely known and this fault was interpreted as a dominantly transpressional, deformation with only local transtension associated with fault bends. A reconstitution assuming an offset of 85 km on the Ganos fault branch [*Armijo et al.*, 2002] yields a surface increase of about 6900 km^2 with, respectively, 3200 km^2 and 3700 km^2 above the deep basins and on the southern shelf margin. This is about 3 times the value we found. Matching those results would imply an average initial crust thickness of 42 km. Other parameters are displacement and slip obliquity. It is possible that the block model overestimates obliquity as it allows very little compression in Ganos Mountain area in the West and Armutlu area in the East, which are actively uplifting. However, this should not result in a large correction as compression in these zones did not result in an observable crustal thickening in the gravity inversion model. More likely, the total 80 km slip assumed in the block model is an overestimate. The thinned domain that we obtain from gravity modeling appears wider than the Marmara Trough and extends southward beneath the shelf, but is not resolved as two distinct zones of extension. The distribution of crustal thickness thus obtained does not support the presence of a large component of localized extension along the southern fault system. Although the presence of active faults scarps running along the Southern Marmara coast between Gemlik Bay and Kapıdağ Peninsula can be argued based on geomorphology, the eastward connection of this fault system to Ganos Fault is unclear. A Southwestward prolongation and connection with the southern branch of the NAF is another possibility [e.g. *Şengör et al.*, 2014] that would produce less extension, and also less displacement along Ganos Fault. It is thus possible that the total extension across the Southern Marmara zone is much smaller than in the block model of *Armijo et al.* [2002]. In fact, in the block model, the extension in the main zone alone is a better match for the extension estimation integrated over the whole Sea of Marmara area we calculated.

5.2. Tectonic regime evolution during the last 5 Myr

A complementary approach is to compare our estimate of finite extension with estimated present day rate of extension from geodesy. Geodetic data cannot constrain the distribution of motion within the Sea of Marmara but the bulk extension of the domain comprised within the same area as the one we selected (see Figure 9) may be calculated from interpolated velocity fields [*Özeren et al.*, 2010]. *Özeren et al.* [In Prep,] computed a velocity field based on the optimization of the minimization of the difference between the No-net-rotation-based velocities and GPS velocities. Calculations based on this velocity field give an extension rate on our surface of 396 $km^2.Myr^{-1}$. Thus, considering the total finite extension calculated before and assuming a stable extension rate similar to the present rate, the Marmara Sea extension could have been formed in 5.3±0.6 Myr. Although this time period could have accommodated a stable extension rate, there is little chance that the fault system and the way the extension was distributed has been steady as

5 Myr is considered as the absolute maximal age for the incursion of the North Anatolian Fault system in the Marmara Sea [*Şengör et al.*, 2005]. In fact, variations with time of the rate, the width of the deformation zone and of the rate of motion are suspected [e.g. *Şengör et al.*, 2005]. *Grall et al.* [2012] identified a progressive change in basin subsidence distribution in the Marmara Central Basin, implying that the zone affected by extension has been wider during some time in the Pliocence, likely in relation with detachment systems identified in seismic reflection data [*Bécel et al.*, 2009]. *Le Pichon et al.* [In Press] propose that a system analogous to the Corinth detachment system was active in the Pliocene between 4.5 and 3.5 Myr, prior to the initiation of the Main Marmara Fault, and accommodated strain at the tip of the propagating North Anatolian Fault. The beginning of this extension phase as described by *Le Pichon et al.* [In Press] lies in the uncertainty range of our evaluation based on present day extension rate and Moho topography. We propose that the extension strain in the Marmara zone has been stable since the Pliocene, maintaining a constant overall regional extension, but that the incursion of the North Anatolian Fault system restructured the distribution of the extension from a wide zone with high-scale detachment to the current situation where extension is carried along the Main Marmara Fault.

For the last 1.5 Myr, considering a stable geological slip rate of 18 mm/yr [*Le Pichon et al.*, In Press] and supposing that the extension was evenly carried along the 200 km long North Marmara Trough, our surface extension rate leads to an extension rate of 2 mm/yr and an angular obliquity of about 6° between velocity vector and local plate boundary orientation.

Based on the repartition of the crust thinning (see Figure 9), we can make a few assumptions on how the purely extensive system was functioning prior to the North Anatolian Fault propagation. We see that there is a striking difference between two zones, delimited approximately by a SW-NE line crossing the eastern tip of the Kapıdağ Peninsula and the Kumburgaz Basin. In the eastern zone, the thinning is stretched all the way to the southern coast line where the crust thickness is only 80 % of our reference thickness. In the western zone, only a small zone centered on the Tekirdağ Basin southern limit shows a crust thickness below 80 % of our reference thickness, and the Main Marmara Fault crosses the zone exactly at the maximum of the thinned zone. In the east, the shifting of the fault in respect of the thinned zone could simply be the effect of the Cinarcik Basin fast subsidence [*Le Pichon et al.*, In Press], originating from the releasing bend [*Kurt et al.*, 2013]. However, a similar situation does not exist in the West as there is no shifting of the thinning toward the Tekirdağ Basin depocenter. We explain this discrepancy by a difference in the setting before the fault propagation. In the west, where evidence of a high-scale detachment is yet to be found, the extension may have been widely distributed on multiple fault zones. Thus, no clear zone of thinning was created. Whereas in the East, detachment functioning [*Bécel et al.*, 2009; *Le Pichon et al.*, In Press] created a tension localized enough for a defined thinned zone to appear. In these zones, the lower crust was weakened by isotherm rising and ductile flows were facilitated. After the propagation of the North Anatolian Fault northern branch, the extension was carried by half pull-apart basins along the fault, north of the thinned zone. But the existence of an earlier thinning in the eastern Marmara zone facilitated the equalization and the spreading of the Moho indentation by ductile flow from the south, maintaining a shift of the thinning location toward the South of fault. In the following parts, we will quantify the ductile flow in the lower crust and try to evaluate if there is indeed a difference in ductile behavior between an eastern and a western zone.

5.3. Ductile flow in the lower crust

Figure 10 illustrates the concept of an equilibrium depth that we will know define. Since the volume extension calculated before corresponds to the sum of the volume of the Marmara basin and of the volume of the indentation made by the Moho in the lower crust, we define Z_{eq} as the depth which divide a mechanical upper crust in which lateral extension compensate the basins volume and a ductile lower crust in which lateral extension compensate the Moho indentation. Thus, it is a boundary through which no vertical crust material flow should occur to accommodate the extension and may correspond to the limit between a brittle upper crust, where extension results from fault behavior, and a ductile lower crust. We found $Z_{eq} = 8650 \pm 600$ m for the whole Sea of Marmara. This would imply a hot lower crust, which is indeed what is observed South of the Main Marmara Fault through shallow Curie-point depth [*Aydin et al.*, 2005], to allow ductile flow transfers.

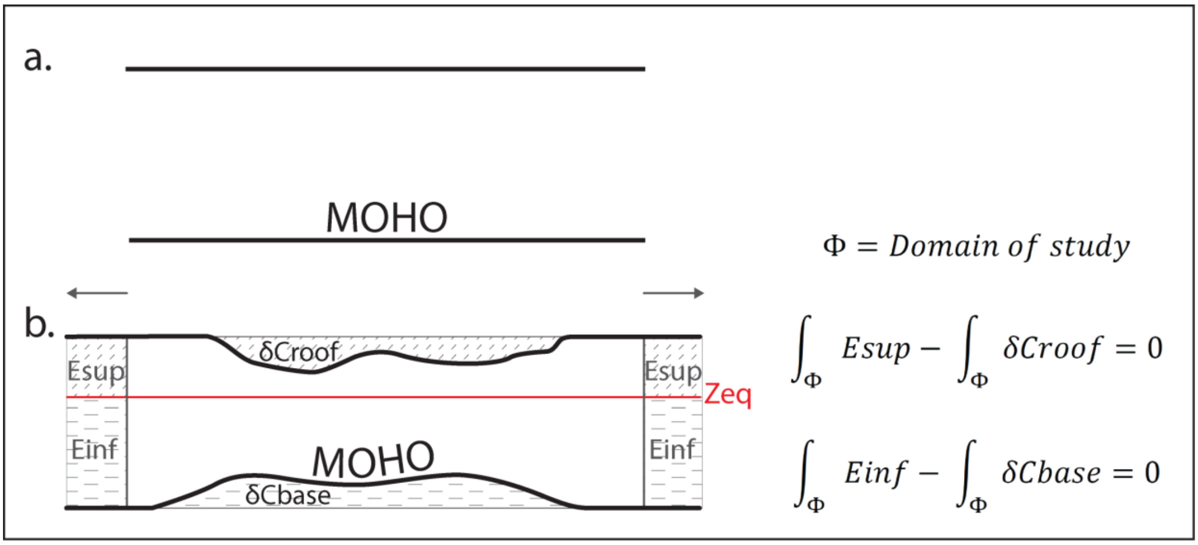

Figure 10. Schematic illustration equilibrium depth concept through which there is no vertical crust material transfer. Considering a constant crust volume we calculate the lateral extension accommodating the thinning. Then, we look for Zeq such as the equations in b. are verified. We found Zeq = 8650±600 m.

To quantify this ductile flow we will now assume that there is no material transfer through Z_{eq} = 8650±600 m and that ductile flow only occurred bellow. Thus, if thinning in the lower crust is not proportionally observed in the upper crust, it must result from lateral material flow in the lower crust. *Figure 11* illustrates this concept and how the reconstitution before extension with constant block volumes deliver the ductile flow between the defined zones.

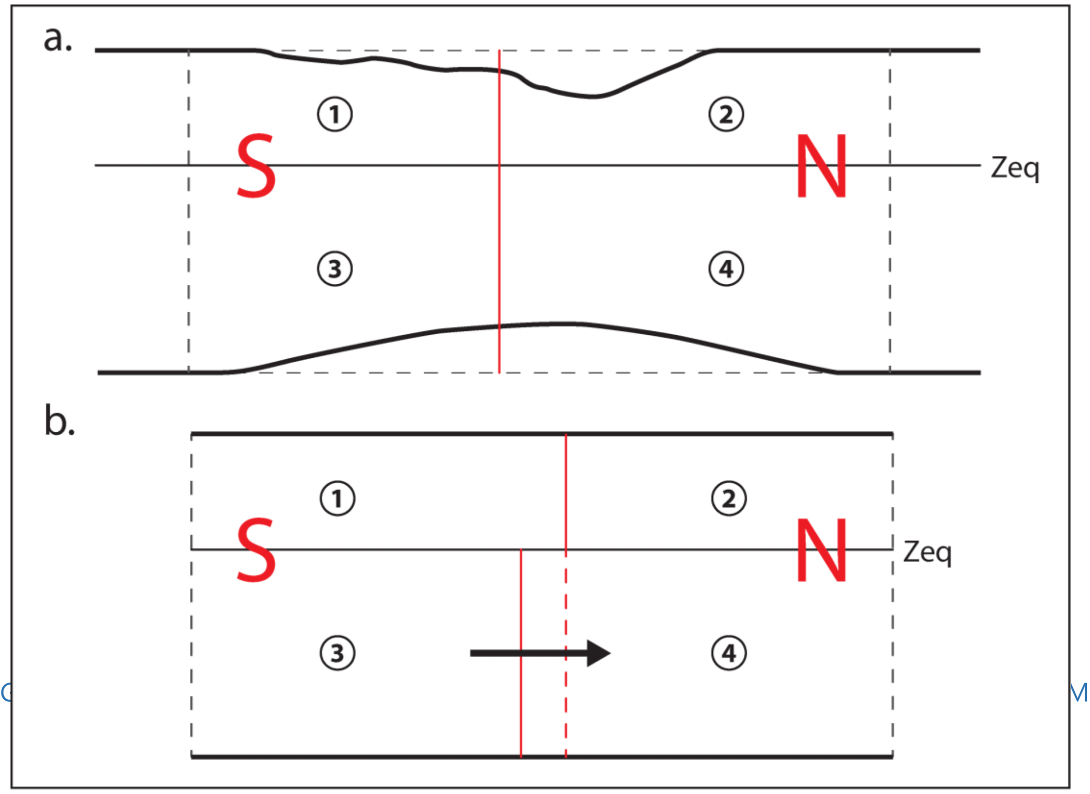

Figure 11. 2D schematic illustration of the crustal material flow rate in the lower crust between a northern and a southern zone. a. Current situation with Zeq the limit through which there is, theoretically, no vertical transfer. The red line delimits a northern and a southern zone. Together with Zeq, it defines four numbered blocks. b. Reconstitution before the extension with constant block volumes. The result gives the direction and the quantity of crust material flow between the Northern and the Southern zone. The dotted line represents the block partition we should observe after reconstitution if there were no lateral transfer in the lower crust. The arrow indicates the direction of crustal flow between the two lower blocks.

We tested this calculation on our domain of study cut at 40.7°N, right between the North Marmara Trough and the southern basins. Calculation gives us the ratio of thinning induced by the northern active zone. We obtain that 14% of total Moho uplift is shifted from North to South in the lower crust. This corresponds to a lateral crust flow toward the Northern zone of 6.3 hm^3. As we constructed the model such that it differentiates two layers in which the extension is carried independently, we can relate this value to the total surface of extension to obtain the surface of extension created by ductile transfer northward in the lower crust. To compute this, we assume that our total of 2100±300 km^2 extension was carried uniformly along the 200 km long Marmara Sea. We finally obtain that, out of about 10.5 km of extension perpendicular to the globally EW direction of the Main Marmara Fault, about1.5 km was associated with norhward ductile lower crust flow toward the Marmara Trough.

In the absence of lower crustal flow, the difference in the ratio of basin volume and Moho uplift volume north and south of 40.7°N could result from different values of equivalence depth on each side of this boundary. Corresponding values would be about 10 km in the north, and 6 km in the south. However, a 6 km brittle layer is probably too thin. Even for a minimum depth of 12 km for the Curie point (580°C), that is reached south of the Sea of Marmara extension zone [*Aydin et al.*, 2005], temperature at 6 km would be less than 290°C.

5.4. Uncertainties

Through our study, we computed uncertainty values induced from two variable parameters: the sediment densities and the reference Moho depth. However, the way the model integrates this depth as an input may not be sufficient to acknowledge the full range of possible uncertainty. In the calculations, the reference depth is the depth at which no gravity anomaly will be created. Thus, the inversion will tend to create a Moho higher than the reference depth if there is a positive anomaly and a Moho lower than the reference depth if there is a negative anomaly. In other words, as our gravity data are relative, the reference depth correspond to the mean gravity value. However, we cannot discard the possibility that a regional thinning, including the Marmara Sea area, occurred during the last 4.5 Myr since the Aegan extension, driven by the Hellenic subduction rollback, has been active for more than 20 Myr [*Jolivet and Faccenna*, 2000]. Thus, a large scale thinning and smoothing by ductile flow in the lower crust may have occurred even though we do observe 30 km as the average value in the region around the Marmara Sea [*Karabulut et al.*, 2013; *Tiberi et al.*, 2001] where no thinning seems to have occurred. In that case, the construction of the Moho variation in regard of a local reference depth would still be valid but a more regional reference depth should be considered in the calculation of overall thinning.

The main other factor that may compromise the accuracy of the Moho topography and of the various calculations based on it is that we did not considered laterally variable densities. As illustrated by *Aydin et al.* [2005], bellow the Sea of Marmara and south of it, Curie point depths are higher than 20 km. As a consequence, higher temperatures and lower densities in the lower crust and in the mantle are expected. This may not be problematic for the application of the Parker method as density variations at interface should not fluctuate significantly, but a thermal gravity correction could deal with gravity anomalies generated by lower densities [*Bai et al.*, 2014]. Since the temperature variations is oriented NS, such a correction would lower the visible divergence in the gravity anomaly before inversion (see Figure 5.) between the North and the South. However, the amplitude of this anomaly is small compared to the anomalies dominating the Marmara Sea area, only a small impact in the final result is expected. However, if this anomaly was corrected before inversion, we would predict a deeper Moho in the North and a relatively higher Moho in the South. This could in part explain the apparently thinner crust in our model beneath the Istanbul block, which appears as a relatively cold zone in the Curie point map [*Aydin et al.*, 2005]. However, the good compatibility with *Karabulut et al.* [2013] profile leaves little room for variations elsewhere.

6. Conclusion

We have presented the result of a gravity anomaly inversion aiming at deciphering the relation between the upper crust tectonic behavior and the lower crust response. Results show that the crust thinning in the Marmara sea area is not limited to the sediment basins location and that lateral ductile flows distributed the thinning away from the mechanically stretched zones in the upper crust. When considering 5 Myr as the initiation of the Neogene extension, the overall surface of extension in the Marmara Sea is compatible with a constant extension rate in the area. However, a reorganization of the tectonic system carrying the extension is likely [eg.: *Şengör et al.*, 2005; *Bécel et al.*, 2009; *Grall et al.* 2012; *Grall et al.*, 2013; *Le Pichon et al.*, In Press].

Acknowledgements

This work was funded by MARSITE FP7 EU project, by COST action FLOW, and by INSU support fund for scientific cruises. We thank the GENAVIR crew during the MARSITE cruise as well as the scientific team for their help and time spent on discussions and explanations during on-board operations. Special thanks to Patrick Le Roy for his detailed presentation of the NO Pourquoi Pas? equipment. We thank Hayrullah Karabulut, Louis Geli, Celal Şengör and, more particularly, Xavier Le Pichon for discussions and constructive comments on the manuscript.

References

Aitken, A. R. A., Salmon, M. L., & Kennett, B. L. N. (2013). Australia’s Moho: A test of the usefulness of gravity modelling for the determination of Moho depth. *Tectonophysics*, *609*, 468–479. doi:10.1016/j.tecto.2012.06.049

Aloisi, G., Soulet, G., Henry, P., Wallmann, K., Sauvestre, R., Vallet-Coulomb, C., … Bard, E. (2015). Freshening of the Marmara Sea prior to its post-glacial reconnection to the Mediterranean Sea. Earth and Planetary Science Letters, 413, 176–185. doi:10.1016/j.epsl.2014.12.052

Armijo, R., Meyer, B., Hubert, A., & Barka, A. (1999). Westward propagation of the North Anatolian fault into the northern Aegean: Timing and kinematics. Geology. doi:10.1130/0091-7613(1999)027<0267:WPOTNA>2.3.CO;2

Armijo, R., Meyer, B., Navarro, S., King, G., & Barka, A. (2002). Asymmetric slip partitioning in the Sea of Marmara pull-apart: a clue to propagation processes of the North Anatolian Fault? Terra Nova, 14(2), 80–86. doi:10.1046/j.1365-3121.2002.00397.x

Aydin, I., Karat, H. I., & Koçak, A. (2005). Curie-point depth map of Turkey. Geophysical Journal International, 162, 633–640. doi:10.1111/j.1365-246X.2005.02617.x

Bai, Y., Williams, S. E., Müller, R. D., Liu, Z., & Hosseinpour, M. (2014). Mapping crustal thickness using marine gravity data: Methods and uncertainties. Geophysics, 79(2), G27–G36. doi:10.1190/geo2013-0270.1

Bayrakci, G., Laigle, M., Bécel, A., Hirn, A., Taymaz, T., Yolsal-Cevikbilen, S., & Team, S. (2013). 3-D sediment-basement tomography of the Northern Marmara trough by a dense OBS network at the nodes of a grid of controlled source profiles along the North Anatolian fault. Geophysical Journal International, 194(3), 1335–1357. doi:10.1093/gji/ggt211

Bécel, A. (2006) Structure Sismique de la Faille Nord Anatolienne en Mer de Marmara, Phd Thesis, Institut de Physique du Globe de Paris.

Bécel, A., Laigle, M., de Voogd, B., Hirn, A., Taymaz, T., Galvé, A., … Özalaybey, S. (2009). Moho, crustal architecture and deep deformation under the North Marmara Trough, from the SEISMARMARA Leg 1 offshore–onshore reflection–refraction survey. *Tectonophysics*, *467*(1-4), 1–21. doi:10.1016/j.tecto.2008.10.022

Bécel, A., Laigle, M., de Voogd, B., Hirn, A., Taymaz, T., Yolsal-Cevikbilen, S., & Shimamura, H. (2010). North Marmara Trough architecture of basin infill, basement and faults, from PSDM reflection and OBS refraction seismics. Tectonophysics, 490(1-2), 1–14. doi:10.1016/j.tecto.2010.04.004

Biddle, K. T., & Christie-Blick, N. (1985). Glossary - Strike-slip deformation, basin formation, and sedimentation. Special Publication of the Society of Economic Paleontologists and Mineralogists, 375–386.

Burchfiel, B. C., & Stewart, J. H. (1966). “Pull-apart” origin of the central segment of Death Valley, California. Geological Society of America Bulletin, 77(April 1966), 439–442. doi:10.1130/0016-7606

Christie-Blick, N., & Biddle, K. T. (1985). Deformation and basin formation along strike-slip faults. Society for Sedimentary Geology, 37, 1–34. doi:10.2110/pec.85.37.0001

De Voogd, B., Serpa, L., & Brown, L. (1988). Crustal extension and magmatic processes: COCORP profiles from Death Valley and the Rio Grande rift. Geological Society of America Bulletin, 100(October), 1550–1567. doi:10.1130/0016-7606(1988)100<1550:CEAMPC>2.3.CO;2

Erickson, S. N., & Jarrard, R. D. (1998). Velocity-porosity relationships for water-saturated siliciclastic sediments. Journal of Geophysical Research, 103, 30385. doi:10.1029/98JB02128

Fliedner, M. M., Ruppert, S., Malin, P. E., Park, S. K., Jiracek, G., Phinney, R. a., … Thompson, G. a. (1996). Three-dimensional crustal structure of the southern Sierra Nevada from seismic fan profiles and gravity modeling. Geology, 24(4), 367–370. doi:10.1130/0091-7613(1996)024<0367:TDCSOT>2.3.CO;2

Gómez-Ortiz, D., & Agarwal, B. N. P. (2005). 3DINVER.M: a MATLAB program to invert the gravity anomaly over a 3D horizontal density interface by Parker–Oldenburg’s algorithm. *Computers & Geosciences*, *31*(4), 513–520. doi:10.1016/j.cageo.2004.11.004

Görür, N., & Okay, a. I. (1996). A fore-arc origin for the Thrace Basin, NW Turkey. *Geologische Rundschau*, *85*(4), 662–668. doi:10.1007/BF02440103

Grall, C., Henry, P., Tezcan, D., Mercier de Lepinay, B., Bécel, A., Geli, L., … Harmegnies, F. (2012). Heat flow in the Sea of Marmara Central Basin: Possible implications for the tectonic evolution of the North Anatolian fault. Geology, 40(1), 3–6. doi:10.1130/G32192.1

Grall, C., Henry, P., Thomas, Y., Westbrook, G. ., Cagatay, M. ., Marsset, B., … Géli, L. (2013). Slip rate estimation along the western segment of the Main Marmara 1 Fault over the last 405-490 ka by correlating Mass Transport Deposits. Tectonics, 32(6), 1587–1601. doi:10.1002/2012TC003255

Hergert, T., & Heidbach, O. (2010). Slip-rate variability and distributed deformation in the Marmara Sea fault system. Nature Geoscience, 3(2), 132–135. doi:10.1038/ngeo739

Hoşgörmez, H., & Yalçın, M. N. (2005). Gas-source rock correlation in Thrace basin, Turkey. *Marine and Petroleum Geology*, *22*(8), 901–916. doi:10.1016/j.marpetgeo.2005.04.002

Jolivet, L., & Faccenna, C. (2000). Meditterranean extension and the Africa-Eurasia collision. Tectonics, 19(6), 1095–1106. doi:10.1029/2000TC900018

Karabulut, H., Schmittbuhl, J., Özalaybey, S., Lengliné, O., Kömeç-Mutlu, a., Durand, V., … Bouin, M. P. (2011). Evolution of the seismicity in the eastern Marmara Sea a decade before and after the 17 August 1999 Izmit earthquake. Tectonophysics, 510(1-2), 17–27. doi:10.1016/j.tecto.2011.07.009

Karabulut, H., Paul, A., Afacan Ergun, T., Hatzfeld, D., Childs, D. M., & Aktar, M. (2013). Long-wavelength undulations of the seismic Moho beneath the strongly stretched Western Anatolia. Geophysical Journal International, 194(1), 450–464. doi:10.1093/gji/ggt100

Katzman, R., Brink, U. S. ten, & Lin, J. (1995). Three-dimensional modeling of pull-apart basins: Implications for the tectonics of the Dead Sea Basin. Journal of Geophysical Research, 100(B4), 6295–6312. doi:10.1029/94JB03101

Kurt, H., Sorlien, C. C., Seeber, L., Steckler, M. S., Shillington, D. J., Cifci, G., … Carton, H. (2013). Steady late quaternary slip rate on the Cinarcik section of the North Anatolian fault near Istanbul, Turkey. Geophysical Research Letters, 40, n/a–n/a. doi:10.1002/grl.50882

Le Pichon, X., Henry, P., & Lallemant, S. (1990). Water flow in the Barbados Accretionary Complex. Journal of Geophysical Research, 95(B6), 8945–8967. doi:10.1029/JB095iB06p08945

Le Pichon, X., Saatc, R., & Tok, B. (2001). The active Main Marmara Fault. Earth and Planetary Science Letters, 192, 595–616.

Le Pichon, X., İmren, C., Rangin, C., Şengör, A. M. C., & Siyako, M. (2013). The South Marmara Fault. International Journal of Earth Sciences, 103(1), 219–231. doi:10.1007/s00531-013-0950-0

Pichon, X., Şengör, A. M. C., Kende, J., İmren, C., Henry, P., Grall, C., & Karabulut, H. (In Press). Propagation of a strike-slip plate boundary within an extensional environment : the westward propagation of the North Anatolian Fault ., 1–98.

Okay, a. I., Satir, M., Zattin, M., Cavazza, W., & Topuz, G. (2008). An Oligocene ductile strike-slip shear zone: The Uludag Massif, northwest Turkey--Implications for the westward translation of Anatolia. Geological Society of America Bulletin, 120(7-8), 893–911. doi:10.1130/B26229.1

Oldenburg, D. W. (1974). The Inversion and interpretation of gravity anomalies. *Geophysics*, *39*(4), 526–536.

Özeren, M. S., & Holt, W. E. (2010). The dynamics of the eastern Mediterranean and eastern Turkey. Geophysical Journal International, 183(3), 1165–1184. doi:10.1111/j.1365-246X.2010.04819.x

Parker, R. L. (1972). The Rapid Calculation of Potential Anomalies. *Geophysical Journal of the Royal Astronomical Society*, *31*(4), 447–455.

Petrunin, A., & Sobolev, S. V. (2006). What controls thickness of sediments and lithospheric deformation at a pull-apart basin? Geology, 34(5), 389–392. doi:10.1130/G22158.1

Rangin, C., Le Pichon, X., Demirbag, E., & Imren, C. (2004). Strain localization in the Sea of Marmara: Propagation of the North Anatolian Fault in a now inactive pull-apart. Tectonics, 23(2), n/a–n/a. doi:10.1029/2002TC001437

Reilinger, R., McClusky, S., Vernant, P., Lawrence, S., Ergintav, S., Cakmak, R., … Karam, G. (2006). GPS constraints on continental deformation in the Africa-Arabia-Eurasia continental collision zone and implications for the dynamics of plate interactions. Journal of Geophysical Research, 111(B5), B05411. doi:10.1029/2005JB004051

Robinson, A., Rudat, J., Banks, C. J., & Wiles, R. L. F. (1996). Petroleum geology of the Black Sea. *Marine and Petroleum Geology*, *13*(2), 195–223. doi:10.1016/0264-8172(95)00042-9

Sandwell, D. T. (1987). Biharmonic s pline interpolation of GEOS-3 and SEASAT altimeter data. *Geophysical Research Letters*, *14*(2), 139–142.

Sandwell, D. T., & Smith, W. H. F. (1997). Marine gravity anomaly from Geosat and ERS 1 satellite altimetry. *Journal of Geophysical Research*, *102*(B5), 10039–10054. doi:10.1029/96JB03223

Sandwell, D. T., Garcia, E., Soofi, K., Wessel, P., Chandler, M., & Smith, W. H. F. (2013). Toward 1-mGal accuracy in global marine gravity from CryoSat-2, Envisat , and Jason-1. *The Leading Edge*, 892–899.

Seeber, L., Emre, O., Cormier, M.-H., Sorlien, C. C., McHugh, C., Polonia, A., … Cagatay, N. (2004). Uplift and subsidence from oblique slip: the Ganos–Marmara bend of the North Anatolian Transform, western Turkey. Tectonophysics, 391(1-4), 239–258. doi:10.1016/j.tecto.2004.07.015

Şengör, A. M. C., Tüysüz, O., İmren, C., Sakınç, M., Eyidoğan, H., Görür, N., … Rangin, C. (2005). the North Anatolian Fault: a New Look. Annual Review of Earth and Planetary Sciences, 33(1), 37–112. doi:10.1146/annurev.earth.32.101802.120415

Şengör, A. M. C., Grall, C., Imren, C., Pichon, X. Le, Görür, N., Henry, P., … Siyako, M. (2014). The geometry of the North Anatolian transform fault in the Sea of Marmara and its temporal evolution: implications for the development of intracontinental transform faults. Canadian Journal of Earth Sciences, 51(February), 222–242. doi:10.1139/cjes-2013-0160

Siyako, M., & Huvaz, O. (2007). Eocene stratigraphic evolution of the Thrace Basin, Turkey. *Sedimentary Geology*, *198*(1-2), 75–91. doi:10.1016/j.sedgeo.2006.11.008

Smit, J., Brun, J.-P., Cloetingh, S., & Ben-Avraham, Z. (2008). Pull-apart basin formation and development in narrow transform zones with application to the Dead Sea basin. Tectonics, 27(6), 1–17. doi:10.1029/2007TC002119

Sobolev, S. V, & Babeyko, A. Y. U. (1994). Modeling of mineralogical composition, density and elastic wave velocities in anhydrous magmatic rocks. *Surveys in Geophysics*, *15*(5), 515–544. doi:10.1007/BF00690173

Tarantola, Albert. (2005). Inverse Problem Theory and Methods for Model Parameter Estimation. *Society for Industrial and Applied Matematics*.

Ten Brink, U. S., Ben-Avraham, Z., Bell, R. E., Hassouneh, M., Coleman, D. F., Andreasen, G., … Coakley, B. (1993). Structure of the Dead Sea pull-apart basin from gravity analyses. Journal of Geophysical Research, 98(B12), 21877. doi:10.1029/93JB02025

Tiberi, C., Diament, M., Lyon-Caen, H., & King, T. (2001). Moho topography beneath the Corinth rift area (Greece) from inversion of gravity data. Geophysical Journal International, 145, 797–808. doi:10.1046/j.1365-246X.2001.01441.x

Vening-Meinesz, F. A. (1931). Une nouvelle méthode pour la réduction isostatique régionale de l’intensité de la pesanteur. *Bulletin Géodésique*, *29*, 33–51.

Wahr, J. (1996). Geodesy and Gravity Class Notes.

Watts, A. B., Karner, G. D., & Steckler, M. S. (1982). Lithospheric flexure and the evolution of sedimentary basin. Philosophical Transactions of the Royal Society A, 305(1489), 249–281. doi:10.1098/rsta.1982.0036

Watts, A. B., & Burov, E. B. (2003). Lithospheric strengh and its relationship to the elastic and seismogenic layer thickness. Earth and Planetary Science Letters, 213, 113–131. doi:10.1016/S0012-821X(03)00289-9

Zuber, M. T., Bechtel, T. D., & Forsyth, D. W. (1989). Effective elastic thicknesses of the lithosphere and mechanisms of isostatic compensation in Australia, 94, 9353–9367. doi:10.1029/JB094iB07p09353